

**Responses to Reviewer 1 (or RC2) on Impact of high-resolution *a priori* profiles on satellite-based formaldehyde retrievals** by Si-Wan Kim, Vijay Natraj, Seoyoung Lee, Hyeong-Ahn Kwon, Rokjin Park, Joost de Gouw, Gregory Frost, Jhoon Kim, Jochen Stutz, Michael Trainer, Catalina Tsai, and Carsten Warneke

We thank the reviewers for the comments that greatly improved the manuscript. Our responses to the reviewer's comments below are highlighted in blue.

1. *A better description of the radiative transfer calculations is needed. It is not clear how some of the most basic parameters needed for a radiative transfer calculation are treated, i.e. geometry and surface reflectance. Clarifications about how the wide spectral range is used is needed.*

→ The missing information is added in the revised manuscript. Solar zenith angles are 52.8°, 16.7°, and 28.8° at 16, 19, 22 UTC, respectively. Relative azimuth angles are 56.6°, 15.5°, 246.1° at 16, 19, 22 UTC, respectively. Viewing zenith angle in VLIDORT is 46.5°. We assume a constant surface reflectance of 0.05 across the domain. The AMF presented in the manuscript is selected at 340 nm similar to the current satellite retrieval. This information is included (Page 11, Line 9 – 19) in the revised manuscript.

2. *The discussion of WRF-Chem validation with CalNex data could be expanded with the detailed description of the methodology used to match PTR-MS and LP-DOAS measurements with WRF-Chem simulations.*

→ More detailed explanations of how the model results are compared with the PTR-MS and LP-DOAS are added. The model results are sampled at the times and locations nearest the observations. The PTR-MS measurement data onboard the P3 aircraft and the sampled model data are averaged at the model spatial resolution (horizontal and vertical) to allow one-to-one comparison of the observations and model results. The LP-DOAS data have been averaged over the upper light path from 35 m AGL (Millikan Library at Caltech) to 225 m AGL (water tank in Altadena) and have been averaged for one hour prior to the comparison with the model results. The model values on the vertical levels

corresponding to 35 m to 225 m AGL are averaged for comparison with the LP-DOAS data. The model value from the 4 km x 4 km horizontal grid cell containing Millikan Library at Caltech is selected for the comparison with the LP-DOAS observations. This information is now included in the revised manuscript (P 7, L 14-18 and P 8, L 13-19).

3. *AMF calculations at 4km x 4km pixels are shown but these are not compared with calculations at coarser resolution. There is no analysis included about the error in AMFs due to the spatial resolution of a priori vertical profile information. It will be good to include such analysis. Furthermore, AMF calculations are affected by other sources of error such as surface reflectance or topography. This should be at least discussed in the text. Some conclusions and suggestions are qualitative and vague and should be backed up by further quantitative analysis.*

→ Operational HCHO retrievals use global model simulations at roughly 1°-3° grid size as *a priori* profiles, which are ~1000 times larger than the spatial resolution in our study (4 km x 4 km). Thus, we include “fine resolution” in the title. Following reviewer’s comments, we added more discussion of this spatial resolution effect in the revised manuscript.

To understand the effect of spatial resolution, we compare the AMF from global model results (at 2° latitude x 2.5° longitude resolution) used as the *a priori* in the Smithsonian Astrophysical Observatory (SAO) OMI formaldehyde retrieval (Gonzalez Abad et al., 2015) with the AMF from this study in the LA Basin. In contrast to the AMF in this study (see Figure 4 in the manuscript), the AMF in the SAO OMI formaldehyde retrieval does not vary much across the Basin and is close to 1 (see Figure R1 below, which is Figure S3 in the Supporting Material). The average AMF from the OMI SAO product for the domain (33.5N-34.5N, 117W-118.5W) is 1.12, while the same domain average AMF from this study is 0.76. Using the AMF in this study, the domain average HCHO column increases by 47%, and up to ~100% at finer scales, compared with the SAO OMI HCHO column. The vertical HCHO profile in the OMI SAO product is almost constant across the domain, while the model profile at 4 km x 4 km resolution varies substantially. This discussion is included in the revised manuscript (P15, L9-P16, L4).

We discuss the spatial resolution effect on the intensity of HCHO plumes quantitatively as suggested by both reviewers. Figure R2 below (Figure 7 in the revised manuscript) demonstrates a scatter of HCHO mixing ratios at 4 km x 4 km resolution on increasingly coarser grid resolutions from 8 km to 300 km. Here the values for these coarser grids are generated from the spatial averages of the original model results at 4 km resolution in this study. The scatter of mixing ratios increases noticeably at grid resolutions  $\geq 20$  km. For example, the mixing ratios at 4 km resolution vary from 1 to 6 ppb while those at 100 km resolution are between 0 and 3 ppb.

Table R1 (Table 1 in the revised manuscript) summarizes the efficiency of capturing the plumes that have HCHO volume mixing ratios (VMRs) greater than the reference values at each spatial grid resolution. Of particular importance are the reference values of 2 ppb and greater for which the AMF is greatly reduced. Table 1 indicates that a grid size  $\leq 12$  km can capture plumes of HCHO with VMRs  $> 4$  ppb or 5 ppb at 4 km with an efficiency of more than 70%. If the grid size is 8 km, plumes of 1-5 ppb are detected with an efficiency of  $\sim 80\%$ . If the grid size is greater than 100 km, it does not capture plumes with VMR  $> 2$  ppb at this urban location. Thus, the AMF using coarse resolutions  $\geq 100$  km is about 1 because of the low HCHO VMR  $< 2$  ppb.

Currently the typical spatial resolution of regional-scale models for the viewing domain of geostationary satellites like TEMPO (e.g., air quality forecast models for the U.S.) is 12-30 km in latitude and longitude. Our recommendation is to select the finest resolution available, and ideally 4 km. Model simulations at 4 km resolution are computationally expensive for a geostationary satellite's viewing domain and high quality model input data may not be readily available at this resolution (e.g., the emission inventory). At a minimum, model simulations at 8-12 km resolution should be tested for their ability to provide *a priori* profiles for next generation environmental geostationary satellite retrievals if computing resources are available.

The above text is included in the revised manuscript (P19, L12- P20, L16).

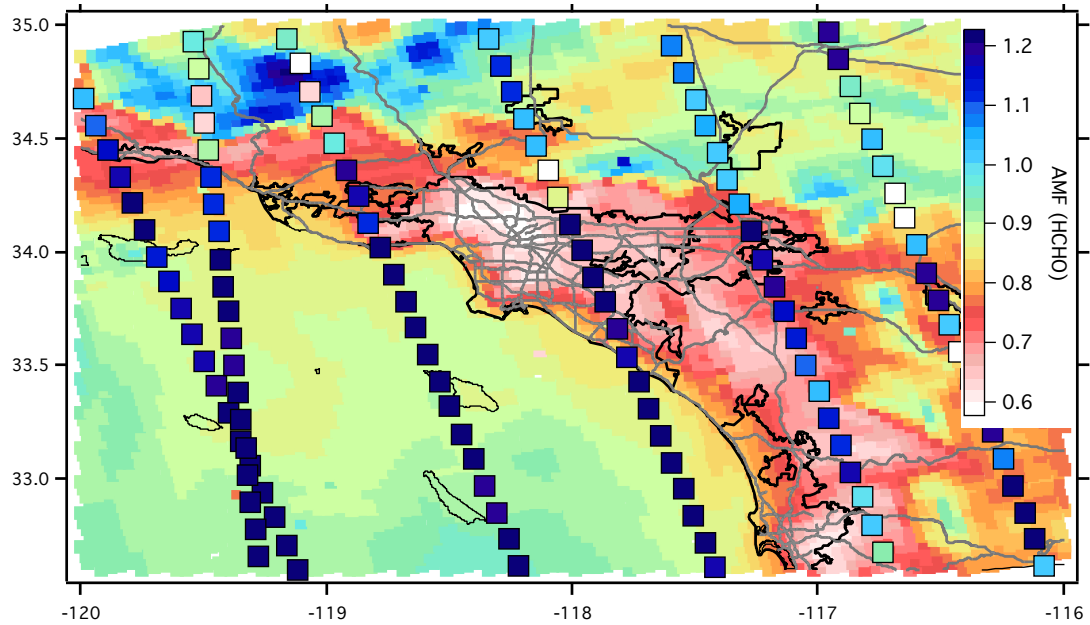


Figure R1. Comparison of the AMF in the OMI operational product (filled square at the center of the OMI swath) with the AMF from this study. An OMI pixel is 24 km x 13 km at nadir and the pixel size increases on either side of this point. The OMI AMF is about 1 on average (blue colors in the color scale used here).



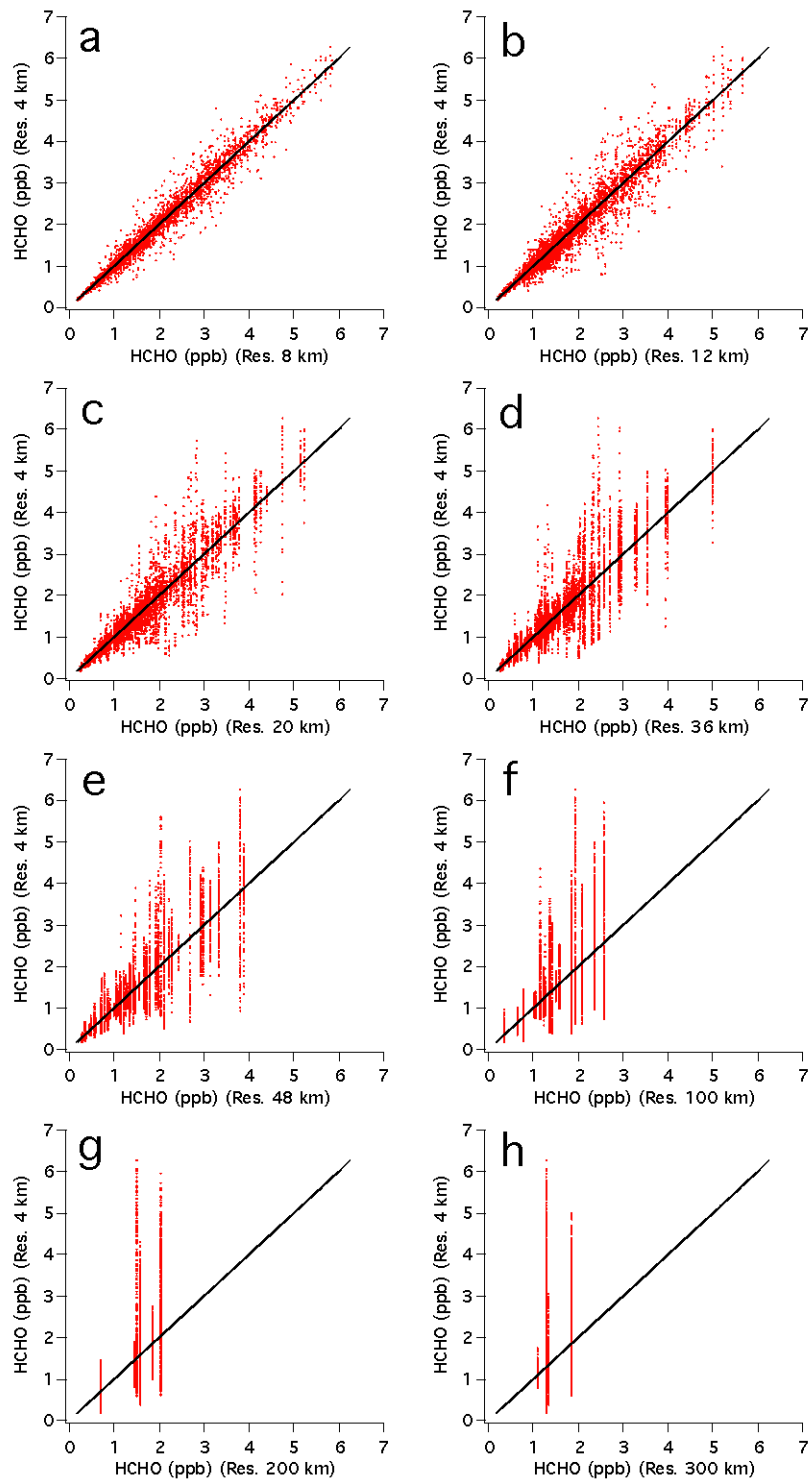


Figure R2. Comparison of HCHO mixing ratios at 4 km x 4 km resolution with mixing ratios at coarser resolutions of (a) 8 km x 8 km, (b) 12 km x 12 km, (c) 20 km x 20 km, (d) 36 km x 36 km, (e) 48 km x 48 km, (f) 100 km x 100 km, (g) 200 km x 200 km, and (h) 300 km x 300 km. The one-to-one line is shown in black.

Table R1. Percentage (%) of intense HCHO plumes retained as the spatial resolution is changed from 4 km. Each column shows the fraction of the plumes retained at coarser resolutions. Here the plume is defined by the area in which the HCHO mixing ratio is greater than the reference HCHO volume mixing ratio (VMR) (1-6 ppb) at 4 km resolution. For example, the second column shows how much area at 8-200 km resolution has a HCHO VMR > 1 ppb when compared with the area with VMR > 1 ppb at 4 km resolution. Similarly, the last column shows how often a model HCHO VMR is greater than 6 ppb at 8-200 km resolution compared with the same plume of VMR > 6 ppb at 4 km resolution; all coarser resolutions (8-200 km) fail to capture this most intense plume. Only model HCHO results at 200 m above ground level at 19 UTC (12 PDT) are used. The areas with HCHO VMRs greater than 1, 2, 3, 4, 5, or 6 ppb are 92800, 29136, 12832, 4256, 848, or 64 km<sup>2</sup>, respectively in the original simulations at 4 km resolution. The area of the domain is 143856 km<sup>2</sup>.

Spatial resolution (km)	Reference HCHO volume mixing ratio (ppb) at 4 km resolution					
	1	2	3	4	5	6
8	98 (%)	95	91	84	79	0
12	97	92	85	73	79	0
20	97	86	72	67	58	0
36	97	82	52	29	0	0
48	96	72	51	0	0	0
100	96	62	0	0	0	0
200	89	56	0	0	0	0
300	53	46	0	0	0	0

4. Section 3.3 doesn't seem to belong to this paper. While it is important to highlight the capabilities of future satellite sensors it is not clear how that example provides any further information about the impact of high-resolution *a priori* profiles in satellite retrievals.

→ The point we are making in this section is that the ability to spatially resolve urban plumes with improved satellite retrievals using fine-resolution *a priori* profiles can provide information relevant to tropospheric ozone chemistry and environmental policy at an urban scale. For example, resolving fine-scale plume structures helps to understand the chemical regimes leading to surface ozone production across the LA basin. We therefore have decided to retain this section in the revised manuscript.

**Abstract:** With the evidence provided in the text the following sentence is not fully supported “Our analyses suggest that an air mass factor (AMF, a factor converting observed slant columns to vertical columns) based on fine spatial and temporal resolution *a priori* profiles can better capture the spatial distributions of the enhanced HCHO plumes in an urban area than the nearly constant AMFs used for current operational products”. High resolution AMFs are not compared with low resolution AMFs.

→ See our response above. We now compare our high resolution AMF with the lower resolution AMF used in the SAO OMI HCHO product. In addition, the effect of spatial resolution on the ability to capture the intensity of HCHO plumes is also included in the revised manuscript.

### Section 2.3:

- At the wavelengths of interest for UV retrievals the surface and atmospheric thermal emission is not relevant. Why are they included in the simulations?

→ The reviewer is correct. We did not include thermal emission. We omitted this sentence in the revised manuscript.

- “We adopt the spectral resolution of 0.2 nm and a spectral range of 300.5 – 365.5 nm”.

Typical formaldehyde satellite retrievals perform AMF calculations at one wavelength ~340nm.

How are the calculations between 300.5 and 365.5 nm used? What is the impact of the 0.2 nm resolution? With typical fitting windows between ~328 nm to ~360 nm why is the ~300 nm to ~328 nm spectral range included?

→ Our calculations are simply done for a spectral range covering wide enough to cover the typical fitting window. We compared the AMF values at several wavelengths and found them to be similar, so we present the AMF at 340 nm in the manuscript.

We initially used a spectral resolution of 0.05 nm. To reduce the computation time, the spectral resolution was reduced from 0.05 nm to 0.2 nm. The spectral resolution did not affect the AMF values we derived in this study.

In the revised manuscript, we clarify the wavelength at which the HCHO AMF is selected and we omit unnecessary notations of “low” and “high” spectral resolution in the plots.

- For each pixel what is the viewing geometry used? Is it assumed the longitude of a geostationary orbit to work out solar, viewing and azimuth angles? This is important information that needs to be included in the description. The similar scattering weights in figure 7 indicate small variations in the viewing geometries (solar angle).

→ As mentioned above, solar zenith angles are 52.8°, 16.7°, and 28.8° at 16, 19, 22 UTC, respectively. Relative azimuth angles are 56.6°, 15.5°, 246.1° at 16, 19, 22 UTC, respectively. Viewing zenith angle in the VLIDORT model is a constant 46.5°. We now specify the information about viewing geometry in the manuscript.

- How is the surface reflectance modelled in the radiative transfer calculations? Is it assumed to be a Lambertian surface with wavelength dependency and time of the day dependency, is it assumed to be a BRDF?

→ To focus on the effect of profile shape, we kept the surface reflectivity constant at 0.05 across the domain. The following text is included in the revised manuscript:

We assume a constant surface reflectance of 0.05 across the domain. For snow-covered mountain top and desert areas, the surface reflectivity can be larger than 0.05, which would increase the sensitivity of satellite HCHO observations to the surface, and in turn would increase the AMF and further modify the spatial distribution of AMF in Southern California. The sensitivity of the

HCHO AMF to the surface reflectivity for this area needs to be pursued in future study using data adequate for the TEMPO HCHO retrieval (P11, L9- P11, L19).

### **Section 3.1:**

- The description about how WRF-Chem and LP-DOAS measurements are collocated and compared should be expanded. There are at least three dimensions that should be considered: horizontal, vertical and temporal. Is the horizontal and vertical sampling of the LP-DOAS measurements accounted for? If so, how? Is there any filtering of LP-DOAS? How is the averaging in the time-domain done?

→ The description of these comparisons is now included in the revised manuscript. See the responses above.

- Likewise for the comparison between WRF-Chem and aircraft data. There is no description about how WRF-Chem simulations and aircraft profiles are matched. It needs to be included to understand the significance of figure 2.

→ The description of these comparisons is now included in the revised manuscript. See the responses above.

**Section 3.2:** As mentioned above these section should include an estimate of the AMF calculations sensitivity with respect to vertical profiles spatial resolution by discussing “high” and “low” spatial resolution cases.

→ In the revised manuscript and responses above, we added a discussion of the effects of varying spatial resolution by comparing with the OMI operational product and by analyzing the sensitivity of HCHO plume detection to the spatial resolution of the model.

- Page 13 line 7: “General features of the AMF distribution in the area do not change significantly when a constant surface pressure is used in the RT simulations (see Supplementary Material Figure S1).” This statement is qualitative. Can it be quantified? How is the vertical distribution of HCHO and other trace gases treated when using a constant surface pressure? Are total columns kept constant? What is the value of that surface pressure? Figure S1 says

“Low Spectral Resolution”. Nowhere in the text it is introduced a “Low Spectral Resolution” or “High Spectral Resolution” calculation.

→ To test the effect of surface pressure, we switched vertical profiles of pressure, temperature, and height in all grid cells with those at one oceanic location (32°N, 120°W) in the input files to VLIDORT. The constant surface pressure value is 1016 hPa. The quantitative analysis of the effect of a constant surface pressure is now included in Figure R3 (Figure S2 in Supporting Material). The differences between the AMF with constant surface pressure and the original AMF are generally less than 10%. 82% (99%) of the domain has AMF differences of less than 5% (10%).

We also added a discussion and quantitative analysis of the impact of the bottom-up emission inventory in the revised manuscript. The spatial pattern of AMF was not strongly affected by the currently available bottom-up emission inventory used to generate the WRF-Chem HCHO profiles in our study (see Supplementary Material Figure S1 and S2). 95% (98%) of the area shows differences in AMF of less than 5% (10%). The impact of the bottom-up emission inventory was larger in Barkley et al. (2012), who compared the effect of using various isoprene emission inventories over tropical South America for satellite HCHO retrievals. In general, Barkley et al. (2012) found an average difference in the HCHO columns of  $\pm 20\%$  and up to 45% in individual locations. The role that the bottom-up emission inventory plays in the AMF calculation therefore depends on the quality (accuracy) of the emission inventories and their impacts on the profile shapes.

Regarding the spectral resolution of VLIDORT, high (low) resolution is 0.05 nm (0.2 nm). For our AMF calculations, this resolution impact is trivial. Following the reviewer’s comment, we omitted the “Low” and “High” portions in the manuscript.

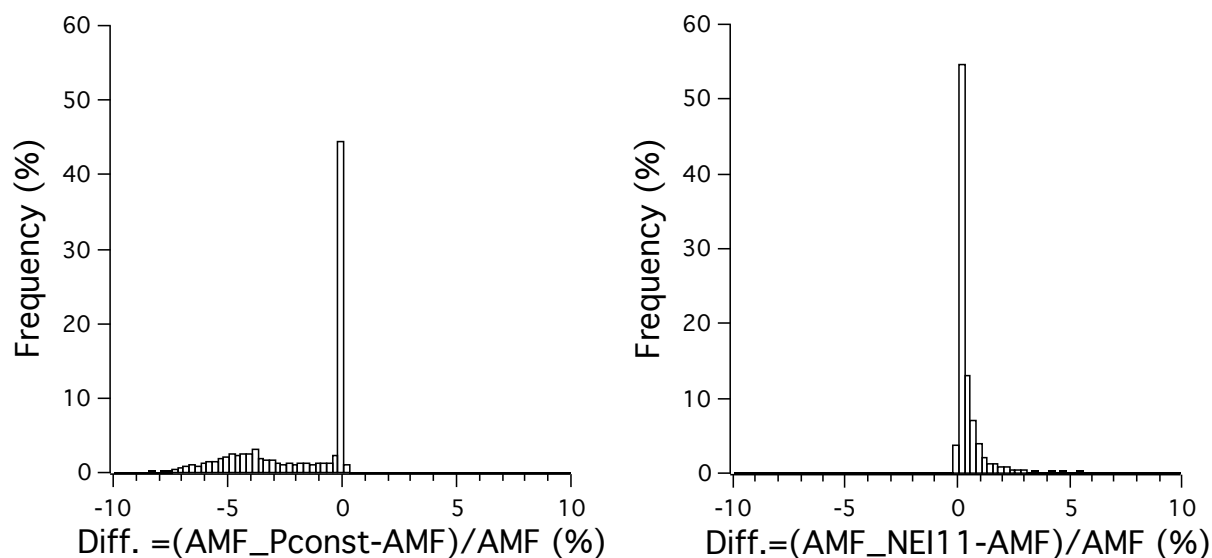


Figure R3. Histogram of (left) differences between the default AMF and the AMF derived using constant surface pressure, and (right) differences between the default AMF and the AMF derived using the NEI11 inventory (with lower VOC emissions than our default inventory) at 19 UTC (12 PDT).

- Page 14 line 17: “The AMF over the ocean increases with time from 0.86 at 09 PDT to 1.03 at 15 PDT as the HCHO mixing ratio decreases with time, probably due to transport of the plume from the ocean to the inland area.” Could be discussed the effect on AMF calculation of the development of the marine boundary layer? Would it be possible to quantify transport using WRF-Chem to support this statement?

→ In response to the reviewer’s suggestion, we analyzed the development of the marine boundary layer and transport. Figure R4 (Figure S5 in Supplementary Material) shows that HCHO mixing ratios above 200 m altitude decrease with time from 06 PDT to 16 PDT. The thermal structure, as shown in the vertical profiles of potential temperature, does not vary much with time. But wind speed changes substantially throughout the day. In the morning, the peak wind speed occurs at ~1.5 km, but the highest wind speeds move lower in altitude (< 500 m) in the afternoon. In the lower atmosphere (altitude < 500 m), wind speed increases during the day from 6 m/s to 15 m/s and wind direction changes from northerly to northwesterly during the same time period. These strong wind changes throughout the day enhance transport of HCHO,

while chemical formation is not high enough to compensate the wind-driven loss of HCHO in this area. This discussion is included in the revised manuscript.

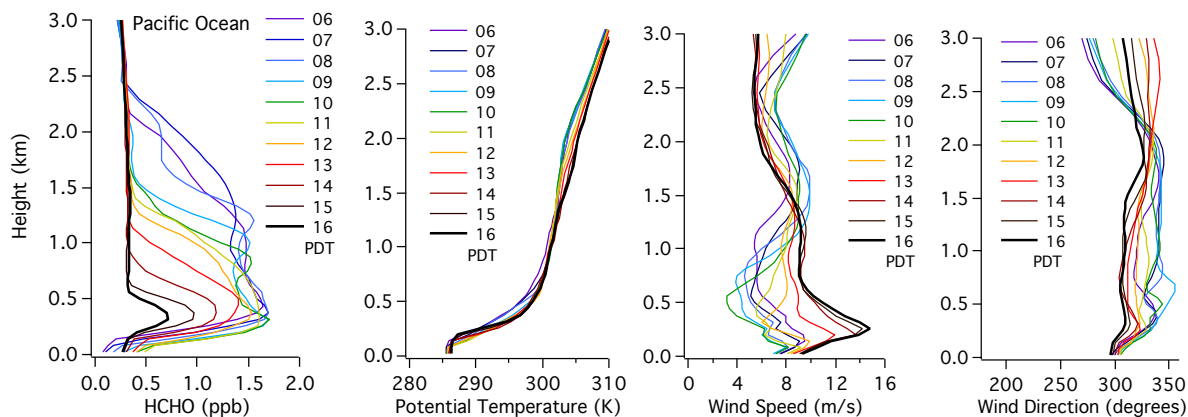


Figure R4. Diurnal variations (06 PDT to 16 PDT) of vertical profiles of HCHO mixing ratio, potential temperature, wind speed, and wind direction over the North Pacific Ocean region.

- Figures 4 and 5: While mixing ratios are interesting, the actual quantity considered in the AMF calculations is the number density. Could that be shown instead?

→ We included the plots in terms of number density below as Figure R5-R7 and in the Supplementary Material (Figure S4, S6, S7). Mixing ratios of HCHO are also widely used. Therefore, we continue to use mixing ratio in the figures of the main text and provide the plots in terms of number density in the Supplementary Material.



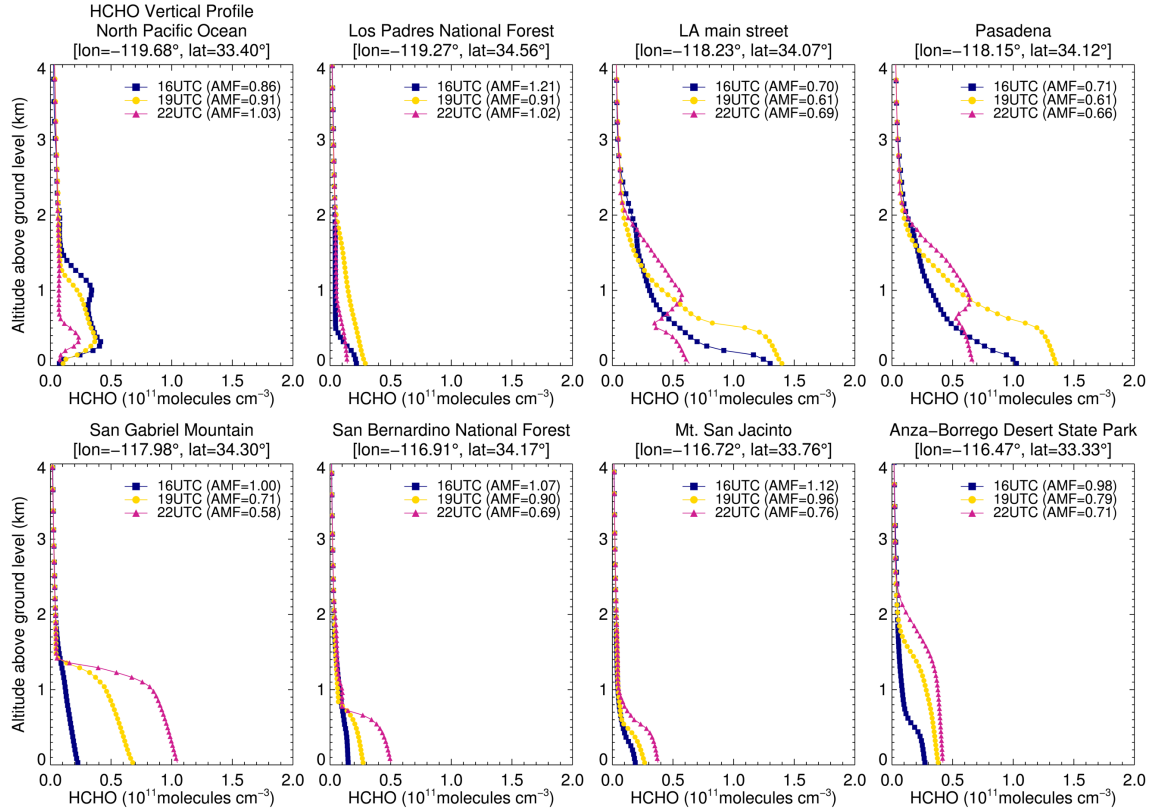


Figure R5. Vertical profiles of HCHO number density are shown for various point of interest, similar to Figure 4 in the main manuscript.

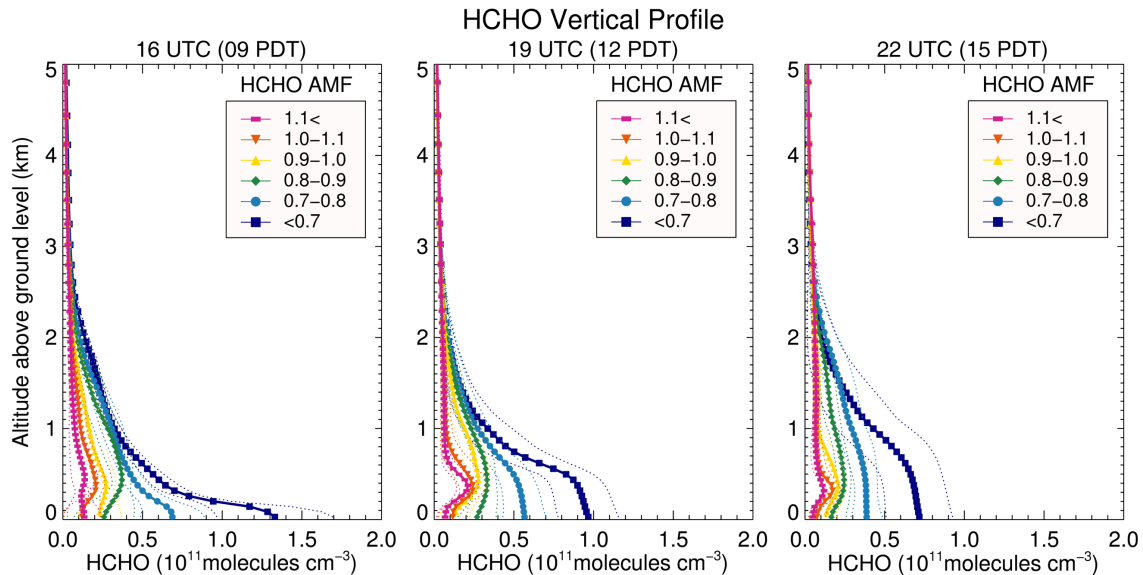


Figure R6. Vertical profiles of HCHO number density averaged for the AMF value intervals (shown in the legends) at 16, 19, and 22 UTC (left to right) as a function of altitude above ground level. Thick lines with symbols are averages and thin dotted lines are one standard deviations. This figure is similar to Figure 5 in the main manuscript except that HCHO number density is shown instead of mixing ratio.

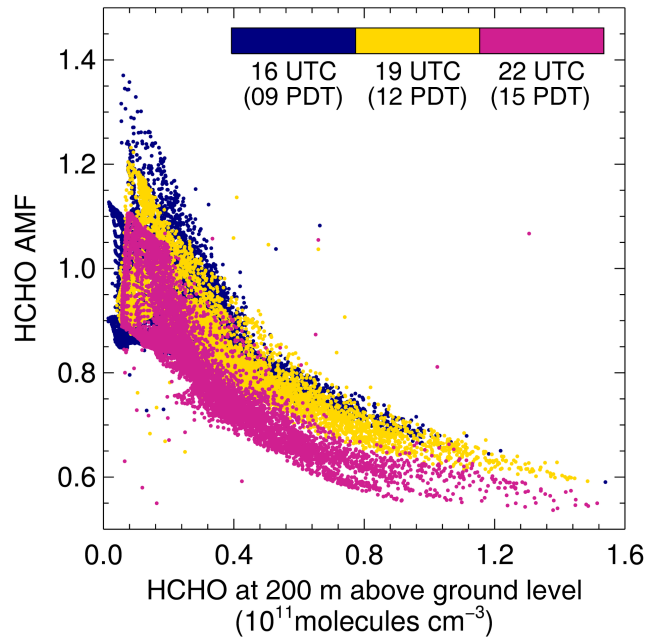


Figure R7. The relationship between the HCHO AMF and model HCHO volume mixing ratio at  $\sim 200$  m altitude. Different colors denote different times. This figure is similar to Figure 6 in the main manuscript except that HCHO number density is shown instead of HCHO mixing ratio.

- Page 15, line 18: “These findings highlight the importance of using time-varying, high spatial resolution a priori profile information for the accurate retrieval of geostationary HCHO measurements.” While there is some quantitative analysis of the importance of using time-varying profiles by showing calculations at 3 different times, there is not such analysis for different spatial resolutions.

→ Discussion of the spatial resolution effect is now included. See our responses above.

- Page 16, line 8: “The dependence of the AMF value on the profile shape is similar at each time of day.” Would it be possible to provide a quantitative analysis backing it up?

→ We modified this section to make the meaning clearer, as follows:

The dependence of the AMF value on the profile shape is similar at each time of day: the higher AMF is related to lower HCHO mixing ratios (or number densities) in the atmospheric boundary layer (up to 1-3 km altitude AGL). More quantitative analysis is shown below.

Using all available data points, we investigate the relationship between AMF and the HCHO mixing ratio at 200 m in the boundary layer at different times of day in Figure 6 [see Figure S7 in Supporting Material for similar plots in terms of number density (molecules  $\text{cm}^{-3}$ )]. Figure 6 illustrates that as the HCHO mixing ratio increases, the AMF decreases. At all times investigated, AMF is anti-correlated with HCHO mixing ratio (or number density). Correlation coefficients between AMF and HCHO mixing ratio are -0.68, -0.85 and -0.84 at 16 (09), 19 (12), and 22 (15) UTC (PDT).

- Page 16, line 13: “For UV-VIS retrievals, it is generally assumed that only the vertical profile shape, rather than the absolute magnitude of the absorber, affects the value of the AMF.” UV-VIS retrievals, as shown in equations 1 and 2, consider the absolute magnitude of the absorber  $\Omega_v$ . It is true that for similar shapes of the vertical distribution of number densities of HCHO columns the values of  $S_z(z)$  will remain constant since it is a normalized quantity. However, a consequence of the atmospheric chemistry, sources and sinks of HCHO is that high total columns and low total columns are generally linked to different shape factors.

→ We agree with the reviewer. The absolute value of HCHO columns (or HCHO concentrations in the boundary layer) is related to the shape factor. Ironically, in general, the accuracy of a priori profile (absolute value) is rather neglected and is not analyzed. Since the original sentence can be misinterpreted, we modified it in the revised manuscript as follows:

For UV-VIS retrievals, it is well known that the vertical profile shape affects the value of the AMF. Our study suggests a strong anti-correlation between the absolute concentration and the AMF: the AMF is low in the area of intense HCHO plumes. The changes in the absolute HCHO concentrations in the boundary layer (altitude AGL < 1-3 km) strongly modify profile shapes, which in turn affect AMF substantially.

- Page 20, line 20: “It is likely that the actual impact of aerosols on the AMF is relatively small when compared with other factors examined here.” This is a qualitative statement that should be backed up with data. Otherwise it should be removed. Kwon et al., 2017 showed the impact of aerosols over East Asia not to be negligible changing columns up to 47%.

→ This statement is supported with Table R2 below (Table 2 in the manuscript), the plots below (Figure R8, also Figure S8 in the Supplementary Material) and additional discussion in the manuscript. We now mention that the impact of aerosols can be large over East Asia and refer to Kwon et al. (2017). The text included in the revised manuscript is as follows:

Although the focus of this manuscript is on the shape factor, we also investigate the impact of aerosol loading on AMF for the 8 sites shown in Figure 4. When the aerosol optical properties from the model results are incorporated in our RT model calculations, the AMF is reduced by ~10% at the N. Main St. and Pasadena sites and by < 10% at other sites (Table 2). The aerosol optical depth, single scattering albedo, and asymmetry factor calculated from the model results for the 8 sites are about 0.5, 0.9, and 0.7, respectively. These are close to the values suggested as the most probable atmospheric conditions in the LA Basin (see Table 4 in Baidar et al., 2013). Because the model aerosol results were not thoroughly evaluated and optimized and only 8 sites were tested, the analysis of aerosol impact in this study is limited. It is possible that some of the simulated aerosol components are overestimated, because the emission inventory is not fully up to date for primary aerosol emissions and aerosol precursor gases (e.g., overestimations of black carbon and SO<sub>2</sub> by a least a factor of 3). Meanwhile, the AMF changes from the values at 16 UTC (09PT) due to diurnal variations in *a priori* profile shape range from -40% to 20% (Table 2). It is likely that the impact of aerosols on the AMF is relatively small when compared with the impact of the profile shape factor examined in this study for the LA basin. De Smedt et al. (2015) and Wang et al. (2017) also reported the importance of *a priori* profile shapes for an improvement of satellite-based HCHO retrievals in Beijing, Xianghe, Wuxi in China. Kwon et al. (2017) demonstrated that the impact of aerosol loading on HCHO AMF can be large over East Asia in contrast to our study for the LA basin.

Table R2. Summary of air mass factors at 8 locations at 16-22 UTC (09-15 PDT). The results without/with aerosols impacts are also shown.

Location	16 UTC (09PDT)		19 UTC (12 PDT)		22 UTC (15 PDT)	
	Aerosol		Aerosol		Aerosol	
	X	O	X	O	X	O
N. Pacific Ocean	0.86	0.75	0.90	0.85	1.03	0.99
Los Padres	1.21	1.15	0.90	0.86	1.02	1.00
Main St.	0.70	0.60	0.61	0.54	0.69	0.62
Pasadena	0.71	0.62	0.60	0.53	0.66	0.58
San Gabriel	1.00	0.93	0.71	0.65	0.58	0.51
San Bernardino	1.07	1.02	0.89	0.86	0.69	0.66
San Jacinto	1.12	1.07	0.95	0.93	0.76	0.73
Anza-Borrego	0.98	0.91	0.79	0.75	0.71	0.66

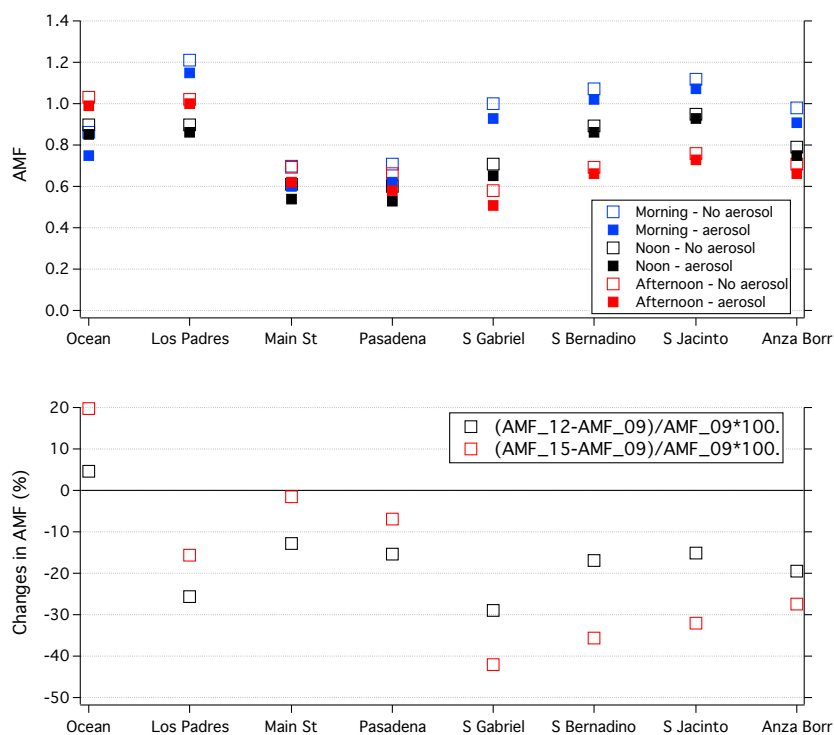


Figure R8. (Top) AMF at 8 sites in the domain at 9, 12, and 15 PDT without/with aerosol impacts. Filled (open) square denote AMF with (without) aerosol impacts. (Bottom) changes in AMF (%) with time. Black (red) open square denotes changes of AMF between 9 and 12 PDT (15PDT).

### Section 3.3:

- Page 21, line 21: “Figure 9 shows 2000-2010 trends in surface O<sub>3</sub> from monitors in Pasadena and San Bernardino.” A brief description of those monitors and their datasets should be added.  
→ We added the information in the revised manuscript. The hourly O<sub>3</sub> data from the South Coast Air Quality Management District (AQMD) monitoring network (<http://www.arb.ca.gov/aqmis2/aqdselect.php>) are utilized for the trend study. Details on standard procedures for maintaining and operating air monitoring stations and specific instrumentations are provided in the CARB air monitoring web manual (<http://www.arb.ca.gov/airwebmanual/index.php>). The locations of the sites and the data are shown in Auxiliary Material in Kim et al. (2016).

Technical comments:

Page 3, Line 2: remove the before sources.

→ “the” is removed.

Page 3, Line 5: Add reference for EPA HAP

→ A reference is added.

Technical Support Document EPA’s 2011 National-scale Air Toxics Assessment, 2011 NATA TSD; United States Environmental Protection Agency: United States, 2015;  
<https://www.epa.gov/sites/production/files/2015-12/documents/2011-nata-tsd.pdf>

Page 3, Line 8: Add reference with HCHO atmospheric chemistry.

→ A reference is added.

Wolfe, G. M., Kaiser, J., Hanisco, T. F., Keutsch, F. N., de Gouw, J. A., Gilman, J. B., Graus, M., Hatch, C. D., Holloway, J., Horowitz, L. W., Lee, B. H., Lerner, B. M., Lopez-Hilifiker, F., Mao, J., Marvin, M. R., Peischl, J., Pollack, I. B., Roberts, J. M., Ryerson, T. B., Thornton, J. A., Veres, P. R., and Warneke, C.: Formaldehyde production from isoprene oxidation across NO<sub>x</sub> regimes, *Atmos. Chem. Phys.*, 16, 2597-2610, <https://doi.org/10.5194/acp-16-2597-2016>, 2016.

Page 3, Line 12: Add reference to X. Jin et al., 2017 doi:10.1002/2017JD026720

→ Jin et al. (2017) is added.

Page 4, Line 10: Add reference to A. Lorente et al., 2017 doi:10.5194/amt-10-759-2017

→ Lorente et al. (2017) is added.

Page 5, Line 10: Add reference for TROPOMI.

→ A reference (Veefkind et al., 2012) is included in the text.

TROPOMI on the ESA Sentinel-5 Precursor: A GMES mission for global observations of the atmospheric composition for climate, air quality and ozone layer applications; Veefkind, J.P, et al. ; *Remote Sensing of Environment* 120 (2012) 70-83

Page 21, Line 11: Add reference to X. Jin et al., as above

→ Jin et al. (2017) is added.

Page 24, Line 2: The “authors think” should be the “authors thank”.

→ Corrected.

Page 25, Line 25: The year of Borbon et al., should be 2013.

→ Corrected.

Page 37, Figure 3: It will be good to include the corresponding PDT values as well.

→ PDT values are added in the figure captions.

Page 41, Figure 7: Where it says slope factor it should say shape factor.

→ Corrected. It is Figure 8 in the revised manuscript.

The comments below do not seem to be relevant to our manuscript. Thus, we did not respond to these comments.

Line 68, please include reference to Razavi et al., 2011 (first HCOOH retrievals from IASI).

Line 71, please include Gonzalez Abad et al., 2009 in ACE-FTS papers.

Line 98, please include citation about IASI CO2 retrievals.

Line 118, correct typo (Pommier et al., 2016).

Line 141, actives to become active.

Line 206, should read “Both biases are however” instead of “Both biases is howeve”

Line 282, please specify which other studies.

Figure 2, include units in plots.

Figure 4, please include units in plots.

### Reference in the response and newly added in the revised manuscript

Baidar, S., Oetjen, H., Coburn, S., Dix, B., Ortega, I., Sinreich, R., and Volkamer, R. (2013), The CU Airborne MAX-DOAS instrument: vertical profiling of aerosol extinction and trace gases, *Atmos. Meas. Tech.*, 6, 719-739, <https://doi.org/10.5194/amt-6-719-2013>.

Barkley, M. P., T. P. Kurosu, K. Chance, I. De Smedt, M. V. Roozendael, A. Arneth, D. Hagberg, and A. Guenther (2012), Assessing sources of uncertainty in formaldehyde air mass factors over tropical South America: Implications for top-down isoprene emission estimates, *J. Geophys. Res.-Atmos.*, 117, D13304, doi:10.1029/2011JD016827.

formaldehyde retrieval, *Atmos. Meas. Tech.*, 8, 19-32, <https://doi.org/10.5194/amt-8-19-2015>.

De Smedt, I., Stavrakou, T., Hendrick, F., Danckaert, T., Vlemmix, T., Pinardi, G., Theys, N., Lerot, C., Gielen, C., Vigouroux, C., Hermans, C., Fayt, C., Veeffkind, P., Müller, J.-F., and Van Roozendael, M. (2015), Diurnal, seasonal and long-term variations of global formaldehyde columns inferred from combined OMI and GOME-2 observations, *Atmos. Chem. Phys.*, 15, 12519-12545, <https://doi.org/10.5194/acp-15-12519-2015>.

De Smedt, I., Theys, N., Yu, H., Danckaert, T., Lerot, C., Compernelle, S., Van Roozendael, M., Richter, A., Hilboll, A., Peters, E., Pederngana, M., Loyola, D., Beirle, S., Wagner, T., Eskes, H., van Geffen, J., Boersma, K. F., and Veeffkind, P. (2017), Algorithm Theoretical Baseline for formaldehyde retrievals from S5P TROPOMI and from the QA4ECV project, *Atmos. Meas. Tech. Discuss.*, <https://doi.org/10.5194/amt-2017-393>, in review.

González Abad, G., Liu, X., Chance, K., Wang, H., Kurosu, T. P., and Suleiman, R. (2015), Updated Smithsonian Astrophysical Observatory Ozone Monitoring Instrument (SAO OMI)

Jin, Xiaomeng, A. M. Fiore, L. T. Murray, L. C. Valin, L. N. Lamsal, B. Duncan, K. Folkert Boersma, I. De Smedt, G. Gonzalez Abad, K. Chance, and G. S. Tonnesen (2017), Evaluating a space-based indicator of surface ozone-NO<sub>x</sub>-VOC sensitivity over midlatitude source regions and application to decadal trends. *J. Geophys. Res.*, 122, 10,439-10,461. <https://doi.org/10.1002/2017JD026720>.



- Lorente, A., Folkert Boersma, K., Yu, H., Dörner, S., Hilboll, A., Richter, A., Liu, M., Lamsal, L. N., Barkley, M., De Smedt, I., Van Roozendaal, M., Wang, Y., Wagner, T., Beirle, S., Lin, J.-T., Krotkov, N., Stammes, P., Wang, P., Eskes, H. J., and Krol, M. (2017), Structural uncertainty in air mass factor calculation for NO<sub>2</sub> and HCHO satellite retrievals, *Atmos. Meas. Tech.*, 10, 759-782, <https://doi.org/10.5194/amt-10-759-2017>.
- US EPA (2015a), Technical Support Document EPA's 2011 National-scale Air Toxics Assessment, 2011 NATA TSD, <https://www.epa.gov/sites/production/files/2015-12/documents/2011-nata-tsd.pdf>.
- Veefkind, J. P., et al. (2012), TROPOMI on the ESA Sentinel-5 Precursor: A GMES mission for global observations of the atmospheric composition for climate, air quality and ozone layer applications. *Remote Sensing of Environment* 120, 70-83.
- Wang, Y., Beirle, S., Lampel, J., Koukouli, M., De Smedt, I., Theys, N., Li, A., Wu, D., Xie, P., Liu, C., Van Roozendaal, M., Stavrou, T., Müller, J.-F., and Wagner, T. (2017), Validation of OMI, GOME-2A and GOME-2B tropospheric NO<sub>2</sub>, SO<sub>2</sub> and HCHO products using MAX-DOAS observations from 2011 to 2014 in Wuxi, China: investigation of the effects of priori profiles and aerosols on the satellite products, *Atmos. Chem. Phys.*, 17, 5007-5033, <https://doi.org/10.5194/acp-17-5007-2017>.
- Wolfe, G. M., Kaiser, J., Hanisco, T. F., Keutsch, F. N., de Gouw, J. A., Gilman, J. B., Graus, M., Hatch, C. D., Holloway, J., Horowitz, L. W., Lee, B. H., Lerner, B. M., Lopez-Hilifiker, F., Mao, J., Marvin, M. R., Peischl, J., Pollack, I. B., Roberts, J. M., Ryerson, T. B., Thornton, J. A., Veres, P. R., and Warneke, C. (2016), Formaldehyde production from isoprene oxidation across NO<sub>x</sub> regimes, *Atmos. Chem. Phys.*, 16, 2597-2610, <https://doi.org/10.5194/acp-16-2597-2016>.

**Responses to Reviewer 2 (or RC1) on Impact of high-resolution *a priori* profiles on satellite-based formaldehyde retrievals** by Si-Wan Kim, Vijay Natraj, Seoyoung Lee, Hyeong-Ahn Kwon, Rokjin Park, Joost de Gouw, Gregory Frost, Jhoon Kim, Jochen Stutz, Michael Trainer, Catalina Tsai, and Carsten Warneke

We thank the reviewers for the comments that greatly improved the manuscript. Our responses to the reviewer's comments below are highlighted in blue.

**General comments**

*The subject of the paper, studying the spatial and temporal variations of a priori HCHO profiles and their impact on AMF, is very relevant for current and future satellite retrievals. For their study, the authors used a regional model with a spatial resolution of 4x4km, at three different time of the day. The use of aircraft profiles and LP DOAS measurement to validate the model is giving to the paper an interesting added value to the paper, although their use is limited. However, while the title and the abstract promise to the reader for an evaluation of this resolution impact, the paper does not provide a quantitative answer. I would expect to get an estimate of the errors on AMF when the resolution is decreased in space or in time, with a distinction between both effects. What minimal model resolution is needed to capture the natural resolution of HCHO in the AMF (based on the model)?*

→ Both reviewers suggested to address the impact of spatial resolution in a quantitative manner. In the revised manuscript, we addressed this issue more in a systematic way. First, we compared the AMF from the SAO OMI HCHO retrieval (Gonzalez Abad et al., 2015) with the AMF in this study. In contrast to inhomogeneous AMF in this study, the AMF in the SAO OMI product does not vary much in the domain and is close to 1 (Figure R1 or Figure S3 in Supplementary Material). The average of AMF from the OMI SAO product for the domain (33.5N-34.5N, 117W-118.5W) is 1.12 while the same domain average of AMF from this study is 0.76. If AMF in this study is used, the HCHO column can increase by 47% on the domain-average (up to ~100% at a finer scale), compared with the OMI HCHO column. The vertical HCHO profile in the SAO OMI product is almost a constant in the domain while the model profile at 4 km x 4 km resolution varies substantially. This discussion is included in the revised manuscript P15, L9-P16, L4. As mentioned in the

responses to the other reviewer's comments, the operational HCHO retrievals adopted global model results at roughly 1°-3° grid size as a priori profile, which are ~1000 times as large as the spatial resolution in our study (4 km x 4 km). Thus, we used "fine resolution" in the title. Second, we analyzed the effect of spatial resolution on capturing HCHO plumes in the basin as the reviewer suggested. Figure 6 shows that AMF values are greatly reduced at HCHO mixing ratio of 2, 3 and 4 ppb. We examined the spatial resolutions at which the HCHO plumes of these critical levels of mixing ratio can be captured. The values for coarse grids (8 km – 300 km) are generated from the spatial averages of the original model results at 4 km resolution. Figure R2 and Table R1 (Figure 7 and Table 1 in the revised manuscript) indicate that the grid size  $\leq 12$  km can capture the plumes of HCHO VMR  $> 4$  ppb or 5 ppb by more than 70%. If the grid size is 8 km, the plumes of 1-5 ppb are detected by ~80%. If the grid size is greater than 100 km, it does not capture the plume of VMR  $> 2$  ppb at this urban location. Thus, the AMF using the coarse resolution  $\geq 100$  km is about 1 because of low concentration that is less than 2 ppb. Currently typical spatial resolution of regional-scale models for the viewing domain of the geostationary satellites (e.g., air quality forecast models for the U.S.) is 12-30 km in each latitude and longitude direction. Our recommendation is to select the resolution as close as 4 km. Since the model simulation at 4 km resolution is computationally expensive for the current geostationary satellite viewing domain and all of high quality input data to the model are not readily available at this resolution (e.g., emission inventory), the model simulations at 8-12 km resolution are recommended to test and improve the model simulations and finally acquire *a priori* profile for next generation environmental geostationary satellite retrievals if computing resources are available. This is included in the revised manuscript P19, L12- P20, L16.

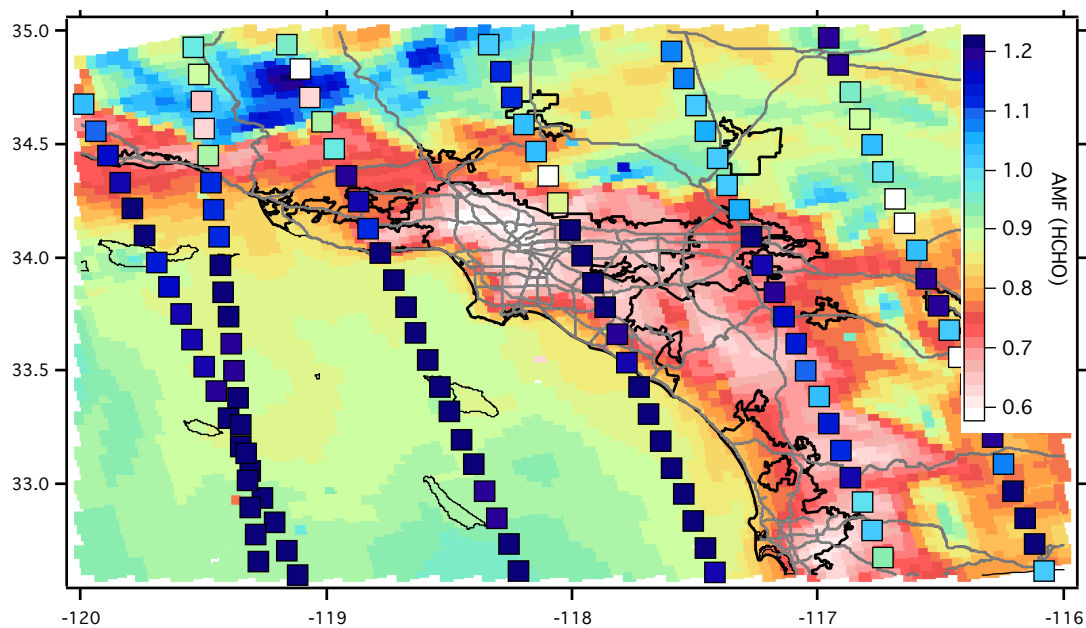


Figure R1. Comparison of the AMF in the OMI operational product (filled square at the center of the OMI swath) with the AMF from this study. An OMI pixel is 24 km x 13 km at nadir and the pixel size increases on either side of this point. The OMI AMF is about 1 on average (blue colors in the color scale used here).

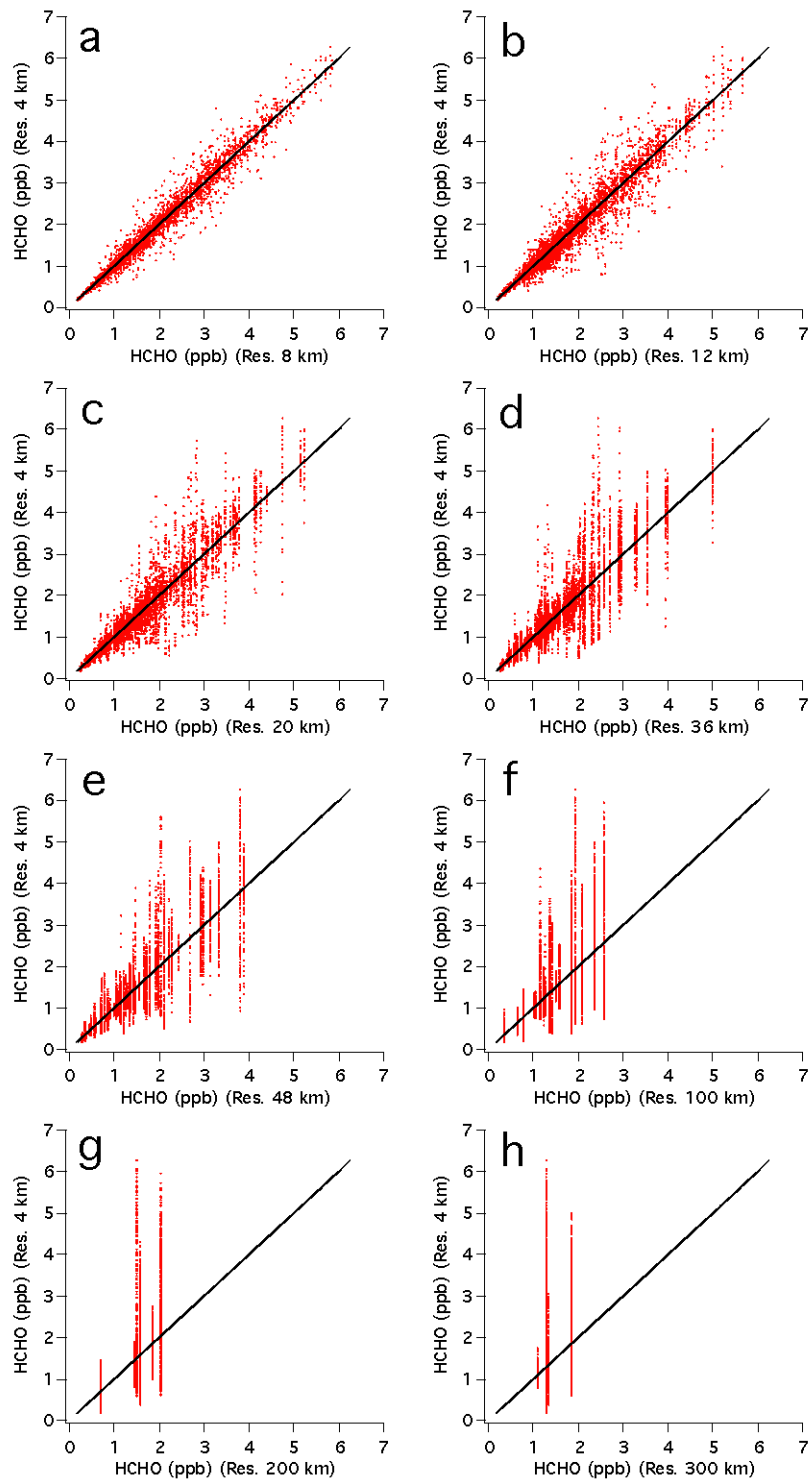


Figure R2. Comparison of HCHO mixing ratios at 4 km x 4 km resolution with mixing ratios at coarser resolutions of (a) 8 km x 8 km, (b) 12 km x 12 km, (c) 20 km x 20 km, (d) 36 km x 36 km, (e) 48 km x 48 km, (f) 100 km x 100 km, (g) 200 km x 200 km, and (h) 300 km x 300 km. The one-to-one line is shown in black.

Table R1. Percentage (%) of intense HCHO plumes retained as the spatial resolution is changed from 4 km. Each column shows the fraction of the plumes retained at coarser resolutions. Here the plume is defined by the area in which the HCHO mixing ratio is greater than the reference HCHO volume mixing ratio (VMR) (1-6 ppb) at 4 km resolution. For example, the second column shows how much area at 8-200 km resolution has a HCHO VMR > 1 ppb when compared with the area with VMR > 1 ppb at 4 km resolution. Similarly, the last column shows how often a model HCHO VMR is greater than 6 ppb at 8-200 km resolution compared with the same plume of VMR > 6 ppb at 4 km resolution; all coarser resolutions (8-200 km) fail to capture this most intense plume. Only model HCHO results at 200 m above ground level at 19 UTC (12 PDT) are used. The areas with HCHO VMRs greater than 1, 2, 3, 4, 5, or 6 ppb are 92800, 29136, 12832, 4256, 848, or 64 km<sup>2</sup>, respectively in the original simulations at 4 km resolution. The area of the domain is 143856 km<sup>2</sup>.

Spatial resolution (km)	Reference HCHO volume mixing ratio (ppb) at 4 km resolution					
	1	2	3	4	5	6
8	98 (%)	95	91	84	79	0
12	97	92	85	73	79	0
20	97	86	72	67	58	0
36	97	82	52	29	0	0
48	96	72	51	0	0	0
100	96	62	0	0	0	0
200	89	56	0	0	0	0
300	53	46	0	0	0	0

*A number of details are missing about how the AMFs are computed beside the a priori profiles?  
Angles, albedo, aerosols?*

→ The missing information is added in the revised manuscript. Solar zenith angles are 52.8°, 16.7°, and 28.8° at 16, 19, 22 UTC, respectively. Relative azimuth angles are 56.6°, 15.5°, 246.1° at 16, 19, 22 UTC, respectively. Viewing zenith angle in the VLIDORT is 46.5°. We assumed a constant surface reflectance of 0.05 across the domain. The AMF presented in the manuscript is selected at 340 nm similar to the current satellite retrieval. This information is included (Page 11, Line 9 – 19) in the revised manuscript.

*I think that the discussion about the shape factor introduce some confusion. I do not agree with the following sentence in the conclusion = “For similar profile shapes, the absolute magnitude of HCHO concentration is also an essential factor in determining the AMF”. The author should clarify the impact of a change at a given altitude, that will modify the shape factor, in opposition to a change at all altitudes (multiplicative factor) that will not modify the shape factor and therefore have no impact on the AMF. See also the detailed comments. I would rather conclude that the AMF are very sensitive to the absolute HCHO mixing ratio in the boundary layer.*

→ We agree. Thank you for your comments. We changed the sentence to “Our study reveals that **the AMF is very sensitive to the absolute HCHO mixing ratio (or number density) in the boundary layer.** Therefore, the absolute magnitude of HCHO concentration in the boundary layer is an essential factor in determining the AMF”.

I recommend publications after these comments have been addressed.

## Detailed comments

*P2, I15: please quantify the statement “can better capture”*

→ We added a quantitative analysis in the sentence. Now it reads “...can better capture the spatial distributions of the enhanced HCHO plumes in an urban area than the nearly constant AMFs used for current operational products **by increasing the columns by ~50% in the domain-average and up to 100% at a finer scale**”.

*P2, I16: This sentence is vague. Which operational product (reference?), what does “nearly constant AMF” mean?*

→ A reference on the SAO OMI HCHO product (Gonzalez Abad et al., 2015) is added. González Abad, G., Liu, X., Chance, K., Wang, H., Kurosu, T. P., and Suleiman, R. (2015), Updated Smithsonian Astrophysical Observatory Ozone Monitoring Instrument (SAO OMI) formaldehyde retrieval, *Atmos. Meas. Tech.*, 8, 19-32, <https://doi.org/10.5194/amt-8-19-2015>.

*P3, I12: please cite Jin, X., Fiore, A. M., Murray, L. T., Valin, L. C., Lamsal, L. N., Duncan, B., Folkert Boersma, K., De Smedt, I., Abad, G. G., Chance, K. and Tonnesen, G. S.: Evaluating a space-based indicator of surface ozone-NO<sub>x</sub>-VOC sensitivity over mid-latitude source regions and application to decadal trends, J. Geophys. Res. Atmos., 439–461, doi:10.1002/2017JD026720, 2017.*

→ Jin et al. (2017) is added in the revised manuscript.

*p4, I6-10: HCHO weak absorption in the UV has an impact on slant column uncertainties. AMF uncertainties do not result from the weak HCHO absorption in the UV. Please clarify.*

→ Agreed. We modified structures of sentences to make the meaning clear. Now it reads as “Because of its weak absorption in the ultraviolet (UV) spectral region, HCHO is regarded as one of the most difficult species to retrieve from satellite-based radiance observations in the UV-visible (UV-VIS) spectral region (e.g., GOME/GOME-2, SCIAMACHY, OMI, and OMPS; see Martin et al., 2003, Zhu et al., 2016 for references). **In addition**, the **large** uncertainties in satellite trace gas retrievals based on UV-VIS spectral measurements arise from the calculation



of the air mass factor (AMF), which converts the slant column density of a trace gas to its vertical column values by considering the vertical sensitivity of the observations (AMF = slant column/vertical column, Palmer et al., 2001; Boersma et al., 2004; Lorente et al., 2017).

**Therefore, it is important to identify factors affecting the accuracy of HCHO retrievals and to find a method to reduce these uncertainties.”**

*P4, l18: add reference to operational products.*

→ Gonzalez Abad et al. (2015) is added in the revised manuscript.

*P4, l16: ..., while the a priori profiles are generally derived from a 3D CTM.*

→ Corrected.

*P4, l18: which operational trace gas products? Please provide reference.*

→ References (Gonzalez Abad et al., 2015; De Smedt et al., 2017) are provided.

De Smedt, I., Theys, N., Yu, H., Danckaert, T., Lerot, C., Compernelle, S., Van Roozendaal, M., Richter, A., Hilboll, A., Peters, E., Pedernana, M., Loyola, D., Beirle, S., Wagner, T., Eskes, H., van Geffen, J., Boersma, K. F., and Veefkind, P.: Algorithm Theoretical Baseline for formaldehyde retrievals from S5P TROPOMI and from the QA4ECV project, Atmos. Meas. Tech. Discuss., <https://doi.org/10.5194/amt-2017-393>, in review, 2017.

*P5, l3-4: references are mixing satellite retrievals and inverse modelling papers.*

→ We modified the sentence. It now reads as “The HCHO retrievals from existing polar-orbiting satellites were investigated and **utilized** in previous studies...”.

*P5, l5-6: It is not clear what is meant by this sentence “these studies .... used the contrast between land and ocean”. Please add more explanations.*

→ This means that the detailed spatial variations in AMF in the US were not captured. We modified the sentence in the revised manuscript. Now it reads “these studies focused on regions with large biogenic sources or **showed large scale contrasts** between land and ocean.”

*P5, l10: Please provide a reference for TROPOMI.*

→ Veefkind et al. (2012) is added in the revised manuscript.

*P5, l15: Recent model provide a resolution of 1x1°, daily (TM5-MP, TROPOMI)*

→ Now it is changed to “horizontal grid resolutions of 1-3 degrees”.

*P13, l1: Please specify to what quantity 35 % refers to. Total AMF, AMF in a certain altitude range?*

→ It meant a change in total AMF. We clarified it. It is changed to “Global Ozone Monitoring Experiment (GOME) measurements that were ~35% less sensitive to the HCHO column (**or 35% smaller total AMF**) over Tennessee than over the North Pacific.”

*P13, l10: please provide a number (relative differences between cases a and b in figure A1) in order to estimate the “small” impact of surface pressure on AMF*

→ Quantitative analyses are shown in the revised manuscript. Please see our response to the other reviewer (Page 9–Page 11).

*P16, l15-16: I do not agree with this discussion. I completely agree that the AMF anti-correlates with the HCHO mixing ratio in the boundary layer. But if the absolute HCHO values changes in the boundary layer, and not at higher altitudes, this changes the profile shape quite strongly.*

→ Agreed. As suggested by the reviewer, we modified the sentences to “For UV-VIS retrievals, it is **well known** that the vertical profile shape affects the value of the AMF. Our study suggests a strong anti-correlation between the absolute concentration and the AMF: the AMF is low in the area of intense HCHO plumes. The changes in the absolute HCHO concentrations in the boundary layer (altitude AGL < 1-3 km) strongly modify profile shapes, which in turn affect AMF substantially.”

*P23, l 8-9: quantify the improvement*

→ In the revised manuscript, we added quantitative analyses in several places. Therefore, we did not change this general conclusion.

*P 23, l8-8: It would be an interesting conclusion to provide a minimum resolution in time and in space, to reduce the AMF uncertainty under a given threshold (ex 10%).*

→ We suggested minimum resolution based on new analysis in Figure 7 and Table 1 (Figure R2 and Table R1 above). Because the simulations at 4 km resolution for the full domain of geostationary environmental satellite are very expensive, it is recommended to use 8-12 km if computing resources are available. More detailed discussions are added in the revised manuscript. See the responses above.

*Figure 1: Specify the dates in the legend*

→ We specified the dates (May-June 2010) in the legend in Figure 1.

*Figure 3: Please improve the visibility of the colorbar and the inset text.*

→ The visibility of the color bar and the text is improved in the revised manuscript.

*Figure 4: The altitude above ground level is not shown in this figure.*

→ The altitude above ground level (or AGL) is noted wherever needed.

*Figure 7: Please do not use “slope” factor. It introduces confusion. You already use profile shape and shape factor.*

→ “slope” factor is changed to “shape” factor in the manuscript and the figure. It is Figure 8 in the revised manuscript.

*After the paper from Palmer et al. 2001, several papers highlighted the importance of the a priori profile shapes on satellite HCHO retrieval: Barkley et al., 2012; De Smedt et al., 2015; Lorente et al., 2017; Wang et al., 2017.*

*Barkley, M. P., Kurosu, T. P., Chance, K. V, De Smedt, I., Van Roozendaal, M., Arneeth, A., Hagberg, D. and Guenther, A. B.: Assessing sources of uncertainty in formaldehyde air mass factors over tropical South America: Implications for top-down isoprene emission estimates, J. Geophys. Res., 117(D13), D13304, doi:10.1029/2011JD016827, 2012.*

De Smedt, I., Stavrakou, T., Hendrick, F., Danckaert, T., Vlemmix, T., Pinardi, G., Theys, N., Lerot, C., Gielen, C., Vigouroux, C., Hermans, C., Fayt, C., Veeffkind, J. P., Müller, J.-F. and Van Roozendael, M.: Diurnal, seasonal and long-term variations of global formaldehyde columns inferred from combined OMI and GOME-2 observations, *Atmos. Chem. Phys.*, 15(8), 12241–12300, doi:10.5194/acpd-15-12241-2015, 2015.

Lorente, A., Folkert Boersma, K., Yu, H., Dörner, S., Hilboll, A., Richter, A., Liu, M., Lamsal, L. N., Barkley, M., De Smedt, I., Van Roozendael, M., Wang, Y., Wagner, T., Beirle, S., Lin, J.-T., Krotkov, N., Stammes, P., Wang, P., Eskes, H. J., and Krol, M.: Structural uncertainty in air mass factor calculation for NO<sub>2</sub> and HCHO satellite retrievals, *Atmos. Meas. Tech.*, 10, 759–782, <https://doi.org/10.5194/amt-10-759-2017>, 2017.

Wang, Y., Beirle, S., Lampel, J., Koukouli, M., De Smedt, I., Theys, N., Li, A., Wu, D., Xie, P., Liu, C., Van Roozendael, M., Stavrakou, T., Müller, J. F. and Wagner, T.: Validation of OMI, GOME-2A and GOME-2B tropospheric NO<sub>2</sub>, SO<sub>2</sub> and HCHO products using MAX-DOAS observations from 2011 to 2014 in Wuxi, China: Investigation of the effects of priori profiles and aerosols on the satellite products, *Atmos. Chem. Phys.*, 17(8), 5007–5033, doi:10.5194/acp-17-5007-2017, 2017

→ Thank you very much for excellent papers. We are glad to include these papers as reference. All of these papers above are referred in the revised manuscript.

### Reference in the response and newly added in the revised manuscript

Baidar, S., Oetjen, H., Coburn, S., Dix, B., Ortega, I., Sinreich, R., and Volkamer, R. (2013), The CU Airborne MAX-DOAS instrument: vertical profiling of aerosol extinction and trace gases, *Atmos. Meas. Tech.*, 6, 719–739, <https://doi.org/10.5194/amt-6-719-2013>.

Barkley, M. P., T. P. Kurosu, K. Chance, I. De Smedt, M. V. Roozendael, A. Arneth, D. Hagberg, and A. Guenther (2012), Assessing sources of uncertainty in formaldehyde air mass factors over tropical South America: Implications for top-down isoprene emission estimates, *J. Geophys. Res.-Atmos.*, 117, D13304, doi:10.1029/2011JD016827.

formaldehyde retrieval, *Atmos. Meas. Tech.*, 8, 19–32, <https://doi.org/10.5194/amt-8-19-2015>.

De Smedt, I., Stavrakou, T., Hendrick, F., Danckaert, T., Vlemmix, T., Pinardi, G., Theys, N., Lerot, C., Gielen, C., Vigouroux, C., Hermans, C., Fayt, C., Veeffkind, P., Müller, J.-F., and Van Roozendael, M. (2015), Diurnal, seasonal and long-term variations of global formaldehyde

- columns inferred from combined OMI and GOME-2 observations, *Atmos. Chem. Phys.*, 15, 12519-12545, <https://doi.org/10.5194/acp-15-12519-2015>.
- De Smedt, I., Theys, N., Yu, H., Danckaert, T., Lerot, C., Compernelle, S., Van Roozendael, M., Richter, A., Hilboll, A., Peters, E., Pedernana, M., Loyola, D., Beirle, S., Wagner, T., Eskes, H., van Geffen, J., Boersma, K. F., and Veefkind, P. (2017), Algorithm Theoretical Baseline for formaldehyde retrievals from S5P TROPOMI and from the QA4ECV project, *Atmos. Meas. Tech. Discuss.*, <https://doi.org/10.5194/amt-2017-393>, in review.
- González Abad, G., Liu, X., Chance, K., Wang, H., Kurosu, T. P., and Suleiman, R. (2015), Updated Smithsonian Astrophysical Observatory Ozone Monitoring Instrument (SAO OMI)
- Jin, Xiaomeng, A. M. Fiore, L. T. Murray, L. C. Valin, L. N. Lamsal, B. Duncan, K. Folkert Boersma, I. De Smedt, G. Gonzalez Abad, K. Chance, and G. S. Tonnesen (2017), Evaluating a space-based indicator of surface ozone-NO<sub>x</sub>-VOC sensitivity over midlatitude source regions and application to decadal trends. *J. Geophys. Res.*, 122, 10,439-10,461. <https://doi.org/10.1002/2017JD026720>.
- Lorente, A., Folkert Boersma, K., Yu, H., Dörner, S., Hilboll, A., Richter, A., Liu, M., Lamsal, L. N., Barkley, M., De Smedt, I., Van Roozendael, M., Wang, Y., Wagner, T., Beirle, S., Lin, J.-T., Krotkov, N., Stammes, P., Wang, P., Eskes, H. J., and Krol, M. (2017), Structural uncertainty in air mass factor calculation for NO<sub>2</sub> and HCHO satellite retrievals, *Atmos. Meas. Tech.*, 10, 759-782, <https://doi.org/10.5194/amt-10-759-2017>.
- US EPA (2015a), Technical Support Document EPA's 2011 National-scale Air Toxics Assessment, 2011 NATA TSD, <https://www.epa.gov/sites/production/files/2015-12/documents/2011-nata-tsd.pdf>.
- Veefkind, J. P., et al. (2012), TROPOMI on the ESA Sentinel-5 Precursor: A GMES mission for global observations of the atmospheric composition for climate, air quality and ozone layer applications. *Remote Sensing of Environment* 120, 70-83.
- Wang, Y., Beirle, S., Lampel, J., Koukouli, M., De Smedt, I., Theys, N., Li, A., Wu, D., Xie, P., Liu, C., Van Roozendael, M., Stavrou, T., Müller, J.-F., and Wagner, T. (2017), Validation of OMI, GOME-2A and GOME-2B tropospheric NO<sub>2</sub>, SO<sub>2</sub> and HCHO products using MAX-DOAS observations from 2011 to 2014 in Wuxi, China: investigation of the effects of priori profiles and aerosols on the satellite products, *Atmos. Chem. Phys.*, 17, 5007-5033, <https://doi.org/10.5194/acp-17-5007-2017>.

Wolfe, G. M., Kaiser, J., Hanisco, T. F., Keutsch, F. N., de Gouw, J. A., Gilman, J. B., Graus, M., Hatch, C. D., Holloway, J., Horowitz, L. W., Lee, B. H., Lerner, B. M., Lopez-Hilifiker, F., Mao, J., Marvin, M. R., Peischl, J., Pollack, I. B., Roberts, J. M., Ryerson, T. B., Thornton, J. A., Veres, P. R., and Warneke, C. (2016), Formaldehyde production from isoprene oxidation across NO<sub>x</sub> regimes, *Atmos. Chem. Phys.*, 16, 2597-2610, <https://doi.org/10.5194/acp-16-2597-2016>.

# Impact of high-resolution *a priori* profiles on satellite-based formaldehyde retrievals

5 Si-Wan Kim<sup>1,2,3</sup>, Vijay Natraj<sup>4</sup>, Seoyoung Lee<sup>3</sup>, Hyeong-Ahn Kwon<sup>5</sup>, Rokjin Park<sup>5</sup>, Joost de Gouw<sup>1,2</sup>, Gregory Frost<sup>1</sup>, Jhoon Kim<sup>3</sup>, Jochen Stutz<sup>6</sup>, Michael Trainer<sup>1</sup>, Catalina Tsai<sup>6</sup>, and Carsten Warneke<sup>1,2</sup>

<sup>1</sup>NOAA Earth System Research Laboratory, Chemical Sciences Division, Boulder, CO 80305,

10 USA

<sup>2</sup>Cooperative Institute for Research in Environmental Sciences, University of Colorado, Boulder, CO, USA

<sup>3</sup>Department of Atmospheric Sciences, Yonsei University, Seoul, South Korea

<sup>4</sup>Jet Propulsion Laboratory, California Institute of Technology, Pasadena, CA, USA

15 <sup>5</sup>Department of Earth and Environmental Sciences, Seoul National University, Seoul, South Korea

<sup>6</sup>Department of Atmospheric Sciences, University of California Los Angeles, CA, USA

20 Correspondence to: Si-Wan Kim ([siwan.kim@noaa.gov](mailto:siwan.kim@noaa.gov))

## Abstract

Formaldehyde (HCHO) is either directly emitted from sources or produced during the oxidation of volatile organic compounds in the troposphere. It is possible to infer atmospheric HCHO concentrations using space-based observations, which may be useful for studying emissions and tropospheric chemistry at urban to global scales depending on the quality of the retrievals. In the near future, an unprecedented volume of satellite-based HCHO measurement data will be available from both geostationary and polar-orbiting platforms. Therefore, it is essential to develop retrieval methods appropriate for the next-generation satellites that measure at higher spatial and temporal resolution than the current ones. In this study, we examine the importance of fine spatial and temporal resolution *a priori* profile information on the retrieval by conducting approximately 45,000 radiative transfer model calculations in the Los Angeles Basin megacity. Our analyses suggest that an air mass factor (AMF, a factor converting observed slant columns to vertical columns) based on fine spatial and temporal resolution *a priori* profiles can better capture the spatial distributions of the enhanced HCHO plumes in an urban area than the nearly constant AMFs used for current operational products **by increasing the columns by ~50% in the domain-average and up to 100% at a finer scale**. For this urban area, the AMF values are inversely proportional to the magnitude of the HCHO mixing ratios in the boundary layer. Using our optimized model HCHO results in the Los Angeles Basin that mimic the HCHO retrievals from future geostationary satellites, we illustrate the effectiveness of HCHO data from geostationary measurements for understanding and predicting tropospheric ozone and its precursors.



## 1. Introduction

Formaldehyde (HCHO) is directly released to the atmosphere from sources that include motor vehicles, industrial activities, prescribed burnings, and wildfires. HCHO is one of the Hazardous Atmospheric Pollutants (HAP) – that are harmful to human health – defined by the US Environmental Protection Agency ([see US EPA 2015a for more information](#)).

More importantly, HCHO is chemically produced during volatile organic compound (VOC) oxidation processes ([Wolfe et al., 2016](#)), and is therefore correlated with major chemical species formed during photochemical smog episodes [e.g., ozone ( $O_3$ )]. Because of the close relationship between HCHO and its VOC precursors, the ratio of satellite HCHO columns to nitrogen dioxide ( $NO_2$ ) columns has been suggested as an indicator of photochemical regimes, i.e., the ratio determines “VOC-limited (or sensitive)” or “ $NO_x$ -limited (or sensitive)” regimes of  $O_3$  formation in a certain location and season (Martin et al., 2004, [Jin et al., 2017](#)). In the presence of  $NO_x$ , HCHO can be a major source of hydroxyl radical (OH), the most important chemical species in the troposphere initiating photochemical chain reactions. The chemical lifetime of HCHO with respect to loss by OH reaction and photolysis is several hours (Warneke et al., 2011). HCHO is highly soluble and may contribute to aqueous chemical processes in clouds and precipitation in the atmosphere and in bodies of water at the Earth’s surface (Barth et al., 2007.; Luecken et al.

2012).

Due to its importance to tropospheric chemistry, atmospheric chemists and the environmental remote sensing community have sought to produce high quality tropospheric HCHO retrievals. Because of its weak absorption in the ultraviolet (UV) spectral region, HCHO is regarded as one of the most difficult species to retrieve from satellite-based radiance observations in the UV-visible (UV-VIS) spectral region (e.g., GOME/GOME-2, SCIAMACHY, OMI, and OMPS; see Martin et al., 2003, Zhu et al., 2016 for references). In addition, the large uncertainties in satellite trace gas retrievals based on UV-VIS spectral measurements arise from the calculation of the air mass factor (AMF), which converts the slant column density of a trace gas to its vertical column values by considering the vertical sensitivity of the observations ( $AMF = \text{slant column} / \text{vertical column}$ , Palmer et al., 2001; Boersma et al., 2004; Lorente et al., 2017). Therefore, it is important to identify factors affecting the accuracy of HCHO retrievals and to find a method to reduce these uncertainties.

Palmer et al. (2001) expressed the AMF as a vertical integral of the product of scattering weight functions and normalized vertical profile shapes of trace gases that vary with atmospheric heights. The scattering weight function can be pre-calculated in a look-up table using radiative transfer (RT) model simulations, while the *a priori profiles* are

generally derived from a three-dimensional chemical transport model. This formulation has been widely used to derive operational trace gas retrieval products (e.g., Gonzalez Abad et al., 2015, De Smedt et al., 2017).

In this study, we examine the role of trace gas vertical profile shapes on HCHO retrievals in the Los Angeles (LA) Basin megacity. The HCHO retrievals from existing polar-orbiting satellites were investigated and utilized in previous studies (e.g., Palmer et al., 2001; Millet et al., 2008; Stavrakou et al., 2015; Abad et al., 2015; Zhu et al., 2016); these studies focused on regions with large biogenic sources or showed large scale contrasts between land and ocean. Zhu et al. (2014) estimated the anthropogenic VOC emissions from large industrial complexes in Houston, Texas, by oversampling OMI HCHO columns. In the near future, HCHO retrievals will be available from both geostationary [e.g., TEMPO (Fishman et al., 2012; Zoogman et al., 2017), GEMS (Kim et al., 2012), Sentinel-4 (Ingmann et al., 2012, Veihelmann et al., 2015)] and polar-orbiting (e.g., TROPOMI, Veeffkind et al., 2012) platforms with much finer temporal and spatial resolutions, enabling satellite-based air quality studies at sub-urban to urban scales. HCHO retrievals at these scales may need a better strategy to deal with spatial and temporal variability in *a priori* vertical profiles of measured tracers than current methods that rely on profile shapes generated by coarse (horizontal grid resolutions of 1-3 degrees) global models. For

example, Heckel et al. (2011) investigated the impacts of the spatial resolution of *a priori* profiles on NO<sub>2</sub> retrievals in a coastal city (San Francisco, California), which highlighted the need for high resolution *a priori* data to quantitatively probe tropospheric pollution in coastal regions and near localized sources such as power plants. Russell et al. (2011) also  
5 found non-negligible impacts of high spatial and temporal resolution terrain and profile inputs on the Ozone Monitoring Instrument (OMI) NO<sub>2</sub> retrievals. Kwon et al. (2017) emphasized the importance of using hourly varying HCHO AMF for geostationary satellite measurements in East Asia mainly due to temporal changes in aerosol chemical composition and vertical distributions.

10 In this study, we simulate fine-resolution (4 km x 4 km) vertical profiles for HCHO retrievals, and investigate the spatiotemporal variability of the HCHO AMF based on these profiles. We also show the usefulness of detailed spatial and temporal information on HCHO plume structures at an urban scale for interpreting the effectiveness of ozone pollution controls.

15

## **2. Data and models**

### **2.1. Aircraft and ground-based measurements**

- *NOAA WP-3 aircraft observations*

During the California Nexus of Air Quality and Climate Change (CalNex) campaign, the NOAA WP-3 aircraft performed 20 research flights mainly over the LA Basin and the Central Valley in California during May and June 2010 (see Ryerson et al., 2013 for more information). The main goals of CalNex were to quantify the emissions of greenhouse gases and ozone and aerosol precursors and to understand the chemical transformations and the transport of pollutants. The NOAA WP-3 aircraft was equipped with a large suite of gas phase and aerosol measurements. In this study, we use the HCHO measurement of a Proton-Transfer-Reaction Mass-Spectrometry (PTR-MS) instrument onboard the WP-3 aircraft (Warneke et al., 2011). Airborne HCHO measurements by PTR-MS are difficult due to a strong humidity dependency. The detection limit for HCHO with this instrument is between 100 pptv in the dry free troposphere and 300 pptv in the humid marine boundary layer. The PTR-MS HCHO measurements have been shown to agree with Differential Optical Absorption Spectroscopy (DOAS) observations (Stutz and Platt, 1997; Platt and Stutz, 2008) within the stated uncertainties. For comparison, the model results are first sampled at the times and locations of the observations. Then the PTR-MS measurement data onboard the P3 aircraft and the sampled model data are averaged at the model spatial resolution (horizontal and vertical) to allow one-to-one comparison of the observations and model results.

20- *UCLA long-path DOAS data in Pasadena during CalNex*

UCLA's long-path (LP) DOAS instrument (Stutz and Platt, 1997; Platt and Stutz, 2008) is located on the California Institute of Technology (Caltech) campus on the roof of the Millikan Library at 35 m AGL (above ground level). Four retro-reflectors are situated northeast of the main instrument in the mountains behind Altadena at 78, 121, 255, and 556 m AGL. The average distance between the LP-DOAS telescope and the reflectors is about 6 km. Spectral retrievals of HCHO mixing ratios were performed in the 324-346 nm wavelength range using a combination of a linear and non-linear least squares fit, as described in Stutz and Platt (1996) and Alicke et al. (2002). Spectral absorption features of O<sub>3</sub>, NO<sub>2</sub>, HONO, O<sub>4</sub>, and HCHO were incorporated in the fitting procedure. The campaign-averaged statistical HCHO error in the DOAS measurements during CalNex was about 150 pptv (Warneke et al, 2011). In the present study, we use these ground-based DOAS data since vertical distribution information resulting from the four retroreflectors at different altitudes allows for comparison with the model results. **The LP-DOAS data are averaged over the upper light path from 35 m AGL (Millikan Library at Caltech) to 225 m AGL (water tank in Altadena) and are averaged for one hour prior to the comparison with the model results. The model values on the vertical levels corresponding to 35 m to 225 m AGL are averaged for the comparison with the LP-DOAS data. The model value from the 4 km x 4 km horizontal grid cell containing Millikan Library at Caltech is selected for the comparison with the LP-DOAS observations.**

20

### *The AQMD surface monitoring data*

The hourly O<sub>3</sub> data from the South Coast Air Quality Management District (AQMD) monitoring network (<http://www.arb.ca.gov/aqmis2/aqdselect.php>) are utilized for the trend study. Details on standard procedures for maintaining and operating air monitoring stations and specific instrumentations are provided in the CARB air monitoring web manual (<http://www.arb.ca.gov/airwebmanual/index.php>). The locations of the sites and the data are shown in Auxiliary Material in Kim et al. (2016).

### **2.2. WRF-Chem model**

We use version 3.4.1 of the Weather Research and Forecasting-Chemistry model (WRF-Chem, Grell et al., 2005). The model physical and chemical settings are the same as that used by Kim et al. (2016). The mother and the nested domains of the WRF-Chem model are the western U.S. (12 km x 12 km horizontal resolution) and the state of California (4 km x 4 km horizontal resolution), respectively. The model has 60 vertical levels with ~50 m thickness between vertical levels up to 4 km above ground level, with coarser vertical resolution at higher levels. The first model level where mixing ratios of chemical species are calculated is ~25 m. The simulation period is 26 April 2010 – 17 July 2010. Meteorological initial and boundary conditions are based on NCEP Global Forecast System data. The MOZART (Model for OZone And Related chemical Tracers, <http://www.acom.ucar.edu/wrf-chem/mozart.shtml>) (Emmons et al., 2010) global model

results are used as initial and boundary conditions for the mother domain of WRF-Chem. Biogenic emissions are based on the Biogenic Emissions Inventory System (BEIS) version 3.13, with additional emissions from urban vegetation (Scott and Benjamin, 2003) are added. The Noah land surface model, YSU planetary boundary layer model, Lin  
5 microphysics scheme, and Grell-Devenyi ensemble cumulus parameterization (only for the mother domain) are adopted (see references in Kim et al., 2009). The chemical mechanism is based on the Regional Atmospheric Chemistry Mechanism (RACM) (Stockwell et al., 1997) with ~30 reaction rate coefficients updated (Kim et al., 2009).

We adopt the NO<sub>x</sub> and CO emission estimates from Kim et al. (2016) that utilized  
10 the fuel-based approaches of McDonald et al. (2012; 2013; 2014). For VOC emissions, we used the emission estimates from the top-down approach employing ground-based observations in Pasadena, as described by Borbon et al. (2013), along with the US EPA NEI05 (US EPA 2008; Kim et al., 2011; 2016) and NEI11 (US EPA 2015b; Ahmadov et al., 2015) inventories. The HCHO model results using the top-down VOC emissions  
15 approach are the focus of this manuscript.

### **2.3. VLIDORT radiative transfer model**

We used the Vector Linearized Discrete Ordinate Radiative Transfer (VLIDORT) model (Spurr, 2008) to calculate a trace gas AMF by vertically integrating the product of the  
20 scattering weight function and the normalized vertical profile function of the trace gas, as



described by Palmer et al. (2001). VLIDORT is a multiple-scattering discrete ordinates RT model for stratified atmospheres. It applies the pseudo-spherical approximation to solve for the multiple scattering of photons in a stratified atmosphere; diffuse scattering is evaluated in a plane-parallel medium, but solar attenuation is performed in a spherical atmosphere. Solar photon single scattering and viewing paths are treated precisely in a spherically curved atmosphere. Since VLIDORT is linearized, simultaneous generation of any number of analytically derived Jacobians with respect to profile quantities, column quantities, or surface properties is possible. We adopt the spectral resolution of 0.2 nm and a spectral range of 300.5-365.5 nm for our HCHO retrievals. The AMF presented in the manuscript is selected at 340 nm, similar to the current satellite retrieval. Solar zenith angles are 52.8°, 16.7°, and 28.8° at 16, 19, 22 UTC, respectively. Relative azimuth angles are 56.6°, 15.5°, 246.1° at 16, 19, 22 UTC, respectively. The viewing zenith angle in VLIDORT is 46.5°. We assume a constant surface reflectance of 0.05 across the domain. For snow-covered mountain top and desert areas, the surface reflectivity can be larger than 0.05, which would increase the sensitivity of satellite HCHO observations to the surface, and in turn would increase the AMF and further modify the spatial distribution of AMF in Southern California. The sensitivity of the HCHO AMF to the surface reflectivity for this area needs to be pursued in future study using data adequate for the TEMPO HCHO retrieval. Vertical profiles of HCHO, O<sub>3</sub>, NO<sub>2</sub>, SO<sub>2</sub>, and BrO mixing ratios were used as inputs to the VLIDORT simulations. We used the WRF-Chem model described above to

generate profiles of HCHO, O<sub>3</sub>, NO<sub>2</sub> and SO<sub>2</sub>, while for BrO, GEOS-Chem global model results were utilized.

### 3. Results

#### 5 3.1. Observed and simulated HCHO

In order to use the model HCHO profiles for AMF calculations and to explore impacts of fine-resolution *a priori* on the retrievals, they should be reasonably good representations of the real atmospheric profiles. Therefore, we evaluate WRF-Chem HCHO simulations with the ground-based LP-DOAS data and aircraft PTR-MS observations. Figure 1 shows  
10 diurnal variations of the near-surface LP-DOAS HCHO observations and model results using various emission inventories on weekdays and weekends. The model results using either the top-down VOC emission estimates based on Borbon et al. (2013; red lines) and the NEI05 (Kim et al., 2016; blue lines) agree with the observations best. The model underestimates the LP-DOAS HCHO observations when we ignore the biogenic VOC  
15 emissions or adopt the most-up-to-date VOC inventory for year 2010 (NEI11, described in Ahmadov et al., 2015), with its lower anthropogenic alkene emissions than those from the NEI05 and top-down approaches. Maximum observed and modeled HCHO mixing ratios in Pasadena are about 4 ppbv during weekdays or 5 ppbv during weekends. During the weekends, faster photochemistry due to lower NO<sub>x</sub> emissions causes higher ozone and  
20 HCHO mixing ratios (Pollack et al., 2012; Kim et al., 2016).

Figure 2 shows the vertical profiles of potential temperature and HCHO mixing ratio from the aircraft observations and model results in the LA Basin on May 4, 2010. The potential temperature profiles in the model agree with the observations and help to characterize different vertical mixing regimes: a stable boundary layer near Catalina Island and the growth of the convective boundary layer from the LA urban cores eastward to the desert on the east side of the Basin. Similarly, the WRF-Chem HCHO profiles are in good agreement with the WP-3 PTR-MS observations. The convective boundary layer develops mainly by buoyancy forcing during daytime and leads to well-defined boundary layer heights (or mixing heights) ranging from a few hundred meters to several kilometers and well-mixed vertical profiles of potential temperature and scalars. Meanwhile, stable boundary layers are characterized by a shallow boundary layer (boundary layer height of maximum a few hundred meters), a positive vertical gradient of potential temperature near the surface, and poorly-mixed vertical profiles of scalars because of weak turbulent mixing that frequently occurs over the ocean or during nighttime. Overall, our model results agree with the observations from the aircraft and ground-based observations; therefore, it is reasonable to use the model HCHO profiles as inputs to VLIDORT and to examine the AMF results from this RT model.

### **3.2. Spatial distribution of AMF and sensitivity to *a priori* profiles at different times of day**

The spatial distribution of the VLIDORT HCHO AMF using the WRF-Chem profiles at 4 km x 4 km resolution at different times of day on May 4, 2010 is shown in Figure 3. The AMF ranges from 0.6 to 1.2 within the LA Basin and in the nearby coastal areas. The AMF values are 0.6-0.7 in the urban cores. In contrast, for high mountains such as the Los Padres Forest located in the northwestern part of the Basin, the AMF is greater than 1. Above the Pacific Ocean near the coast, the AMF is about 0.9-1. These results are similar to the AMF calculations by Palmer et al. (2001); they obtained AMF = 0.71 in Tennessee, where high isoprene levels are seen in the boundary layer, and AMF = 1.1 over the North Pacific. The AMF values calculated by Palmer et al. (2001) resulted in Global Ozone Monitoring Experiment (GOME) measurements that were ~35% less sensitive to the HCHO column (or 35% smaller total AMF) over Tennessee than over the North Pacific. Palmer et al. (2001) also noted small AMF values over California, which they attributed to a shallow boundary layer resulting from strong subtropical subsidence combined with a strong surface source of HCHO from biogenic hydrocarbons. Our study agrees with this finding, except that both anthropogenic and biogenic VOC contribute to high formaldehyde in the LA Basin (Figure 1). General features of the AMF distribution in the area do not change significantly when a constant surface pressure is used in the RT simulations (see Supplementary Material Figure S1 and S2). 82% (99%) of the area shows the differences of AMF less than 5% (10%). The direct influence of complex terrain height on the AMF is small. Similarly, the spatial pattern was not strongly affected by the currently available bottom-up emission

inventory used to generate the WRF-Chem HCHO profiles in our study (see Supplementary Material Figure S1 and S2). 95% (98%) of the area shows the differences of AMF less than 5% (10%). The impact of bottom-up emission inventory was larger in Barkley et al. (2012) when various isoprene emission inventory over tropical South America were included in the satellite HCHO retrievals: in general, the difference in the HCHO columns was  $\pm 20\%$  and for individual locations, it was up to  $\pm 45\%$ . Thus, the role the bottom-up emission inventory play in the AMF calculation varies depending on the quality (accuracy) of the emission inventories and their impacts on the profile shapes.

As mentioned above, the most operational HCHO retrievals adopted global model results at roughly  $1^\circ$ - $3^\circ$  grid size as a priori profile, which are  $\sim 1000$  times as large as the spatial resolution in our study (4 km x 4 km). For the domain of interest in this study, the global model has just a few profiles. Here we compare the AMF from global model results ( $2^\circ$  latitude x  $2.5^\circ$  longitude resolution) as *a priori* in the Smithsonian Astrophysical Observatory (SAO) OMI formaldehyde retrieval (Gonzalez Abad et al., 2015) with the AMF from this study for the LA basin and discuss more on the spatial resolution effect. In contrast to the AMF in this study as in Figure 4, the AMF in SAO OMI formaldehyde retrieval does not vary much in the basin and is close to 1 (see Figure S3 in Supporting Material for details). The average of AMF from the OMI SAO product for the domain (33.5N-34.5N, 117W-118.5W) is 1.12 while the same domain average of AMF from this study is 0.76. If AMF in this study is used, the HCHO column can increase by 47% on the

domain-average (up to ~100% at a finer scale), compared with the OMI HCHO column. The vertical HCHO profile in the OMI SAO product is almost a constant in the domain while the model profile at 4 km x 4 km resolution varies substantially. We will discuss the spatial resolution effect on the intensity of HCHO plumes in depth later.

5 Geostationary satellites such as TEMPO (Fishman et al., 2012; Zoogman et al., 2017), GEMS (Kim et al., 2012), and Sentinel-4 (Ingmann et al., 2012; Veihelmann et al., 2015) are expected to provide diurnally varying information about tropospheric pollution during daytime. It is, therefore, useful to investigate if diurnally varying *a priori* profile information is needed for accurate retrievals of satellite-based HCHO columns. Figure 3

10 shows the spatial distribution of VLIDORT HCHO AMF using the WRF-Chem profiles at 16, 19, and 22 UTC (equivalent to 9, 12, 15 Pacific Daylight Time, PDT, respectively) and HCHO columns. Overall, similar patterns of the AMF distribution are shown at all times: low AMFs in the urban cores and high AMFs in the area of Los Padres National Forest located in the northwestern region of the Basin. However, there are noticeable diurnal

15 changes in the AMFs over the high terrain east and northeast of downtown LA and over the Pacific Ocean near the coast, due to changing photochemical production and destruction and transport of HCHO throughout the day (Figure 3). Overall, minimum AMF values are reduced between morning and afternoon as HCHO is photochemically produced. At 15 PDT, AMF values  $< 0.6$  (the white shading in Figure 3) occur in the mountainous

regions, including the San Gabriel Mountains, San Bernardino National Forest, Mt. San Jacinto, and Anza-Borrego Desert State Park. Onshore transport of photochemically produced HCHO plumes from downtown LA to the mountains occurs in the afternoon (see HCHO columns in Figure 3).

5           Figure 4 shows vertical distributions of the model HCHO mixing ratios at several locations in the LA Basin and the Pacific Ocean for the AMF values at different times of day [see Figure S4 in Supporting Material for the plots with number density unit (molecules  $\text{cm}^{-3}$ )]. Over the Pacific Ocean, the HCHO mixing ratio is small near the surface and more abundant at higher altitudes. The AMF over the ocean increases with time from 0.86 at 09  
10   PDT to 1.03 at 15 PDT as the HCHO mixing ratio decreases with time, probably due to transport of the plume from the ocean to the inland area (see Supporting Material Figure S5 for detailed analyses). Over the land, the HCHO mixing ratio is higher in the boundary layer than in the free atmosphere. In the Los Padres National Forest where the highest AMF (0.91-1.21) occurs, the boundary layer grows with time, but the mixing ratio of HCHO is  
15   small ( $< 1$  ppbv). In Pasadena and at the LA Main St. site, the boundary layer heights and HCHO mixing ratios increase from 9 PDT to 12 PDT. The maximum HCHO value in the boundary layer is about 6 ppbv. The HCHO in the boundary layer decreases at 15 PDT, but mixing ratios above the boundary layer ( $> 1$  km) increase due to the upper level easterly

transport of the HCHO plumes. Consequently, the AMF decreases from 0.7 at 9 PDT to 0.6 at 12 PDT and then increases to 0.7 at 15 PDT, due to an enhanced sensitivity to increased upper-level HCHO mixing ratios. For these urban core sites, the HCHO AMF ranges from 0.6 to 0.7. In the San Gabriel Mountains, San Bernardino National Forest, and Mt. San Jacinto, the boundary layer height is well defined and shallow and does not change significantly throughout the day. However, the AMF values change substantially (decreasing by ~40%) throughout the day over these locations; this is likely because HCHO mixing ratios increase between morning and afternoon, mainly due to transport and formation of the plumes originating from urban core regions. The AMF at Anza-Borrego Desert State Park decreases with time from 0.96 at 9 PDT to 0.71 at 15 PDT due to increasing HCHO mixing ratios, in spite of the increase in boundary layer height. These findings highlight that the importance of using time-varying, high spatial resolution *a priori* profile information for the accurate retrieval of geostationary HCHO measurements.

We extended this analysis in Figure 5, where for ranges of HCHO AMF (e.g., 1.0 < AMF < 1.1) across the model domain, the model HCHO profiles are averaged and plotted at the three times (9, 12, 15 PDT) [see Figure S6 in Supporting Material for the plots with number density unit (molecules  $\text{cm}^{-3}$ )]. Each plot shows that the AMF values are smaller when the HCHO mixing ratios are higher near the surface. At 12 and 15 PDT, as expected,



the profiles have more well-mixed shapes for deeper vertical layers. The dependence of the AMF value on the profile shape is similar at each time of day: the higher AMF is related to lower HCHO mixing ratios (or number densities) in the atmospheric boundary layer (up to 1-3 km altitude AGL). More quantitative analysis is shown below.

5           Using all available data points, we investigate the relationship between AMF and the HCHO mixing ratio at 200 m in the boundary layer at different times of day in Figure 6 [see Figure S7 in Supporting Material for the plots with number density unit (molecules  $\text{cm}^{-3}$ )]. The plot illustrates that as the HCHO mixing ratio increases, the AMF decreases. At all times investigated, AMF is anti-correlated with HCHO mixing ratio (or number  
10   density). Correlation coefficients between AMF and HCHO mixing ratio are -0.68, -0.85 and -0.84 at 16 (09), 19 (12), and 22 (15) UTC (PDT). In general, AMF values decrease from morning to late afternoon. The AMF values are reduced substantially for HCHO mixing ratio of 2, 3, and 4 ppb. Therefore, it is useful to examine if the HCHO mixing ratios of 2, 3, and 4 ppb or higher can be captured at coarser spatial resolutions. Figure 7  
15   demonstrates a scatter of HCHO concentrations at 4 km x 4 km resolution on a coarser grid from 8 km to 300 km. Here the values for coarse grids are generated from the spatial averages of the original model results at 4 km resolution in this study. A scatter of concentrations is getting larger at a spatial grid size  $\geq 20$  km. For example, the concentration at 4 km resolution varies from 1 to 6 ppb while that at 100 km resolution is  
20   about 2 ppb. Table 1 summarizes the efficiency of capturing the plumes that have greater

HCHO mixing ratio than the reference values for each spatial grid resolution. Of particular importance are the reference values of 2, 3, 4 ppb for which AMF is greatly reduced. Table 1 indicates that the grid size  $\leq 12$  km can capture the plumes of HCHO VMR  $> 4$  ppb or 5 ppb at 4 km by more than 70%. If the grid size is 8 km, the plumes of 1-5 ppb are detected by  $\sim 80\%$ . If the grid size is greater than 100 km, it does not capture the plume of VMR  $> 2$  ppb at this urban location. Thus, the AMF using the coarse resolution  $\geq 100$  km is about 1 because of low concentration  $< 2$  ppb. Currently typical spatial resolution of regional-scale models for the viewing domain of the geostationary satellites (e.g., air quality forecast models for the U.S.) is 12-30 km in each latitude and longitude direction. Our recommendation is to select the resolution as close as 4 km. Since the model simulation at 4km resolution is computationally expensive for the current geostationary satellite viewing domain and all of high quality input data to the model are not readily available at this resolution (e.g., emission inventory), the model simulations at 8-12 km resolution are recommended to test and improve the model simulations and finally acquire *a priori* profile for next generation environmental geostationary satellite retrievals if computing resources are available.

For UV-VIS retrievals, it is well known that the vertical profile shape affects the value of the AMF. Our study suggests a strong anti-correlation between the absolute concentration and the AMF: the AMF is low in the area of intense HCHO plumes. The changes in the absolute HCHO concentrations in the boundary layer (altitude AGL  $< 1-3$

km) strongly modify profile shapes, which in turn affect AMF substantially. To understand the importance of the absolute magnitude of HCHO mixing ratios within the context of the mathematical formula of AMF used, we examine shape factor, scattering weight function, and AMF quantitatively. According to Palmer et al. (2001), AMF is expressed as

5

$$AMF = AMF_G \int_0^{\infty} w(z) S_z(z) dz. \quad (1)$$

Here  $AMF_G$  is a geometric air mass factor that is a function of solar zenith angle and satellite viewing angle,  $w(z)$  is a scattering weight that is associated with the sensitivity of the backscattered spectrum to the abundance of the absorber at altitude  $z$ , and  $S_z(z)$  is a vertical shape factor for the absorber representing a normalized vertical profile of number density. The vertical shape factor is defined as

10

$$S_z(z) = \frac{n(z)}{\Omega_v} \quad (2)$$

15

, where  $n(z)$  is the number density (molecules  $\text{cm}^{-3}$ ) at altitude  $z$  and  $\Omega_v$  is the vertical column density or column (molecules  $\text{cm}^{-2}$ ) of HCHO. In this manuscript, AMF in Equation (1) is vertically integrated to the top of model domain that is roughly the top of

troposphere or above. Therefore, AMF here is tropospheric AMF. To understand the sensitivity of AMF on the vertical distribution, we also define  $\Delta AMF_i$ , a discrete increment of AMF for each model layer.

$$5 \quad \Delta AMF_i = AMF_G w_i S_{zi} \Delta z_i \quad (3)$$

, where  $i$  is an index representing the vertical grids,  $\Delta z_i$  is the layer depth for the grid  $i$ , and  $\sum \Delta AMF_i = AMF$ .

In Figure 8, the vertical shape factor in Equation (2), the scattering weight  
 10 (multiplied by geometric AMF), and  $\Delta AMF_i$  are plotted as a function of height over the North Pacific Ocean, San Gabriel Mountains, and Anza Borrego Desert State Park at 16, 19, and 22 UTC (see Figure 4 for the locations of these sites). The differences in the shape factor over the North Pacific Ocean are clear at altitudes  $> \sim 1000$  m: the shape factor values at 22 UTC are larger than those at 16 and 19 UTC. In contrast, the HCHO column at 22  
 15 UTC is smaller than those at 16 and 19 UTC over the ocean (Figure 4). As the column density value decreases, the shape factor above  $\sim 1000$  m becomes larger and causes higher  $\Delta AMF_i$  and (tropospheric) AMFs, because a column density value is used as a normalization parameter for a shape factor. In order words, the satellite measurement is

more sensitive to the profile at 22 UTC than that at 16 UTC at this point over the Pacific Ocean.

For the San Gabriel Mountain site, the HCHO is confined below ~1400 m at 16, 19, and 22 UTC (there are no significant changes in boundary layer height during this time period) and its mixing ratio increases with time (Figure 4). The shape factor at 19 and 22 UTC is higher than that at 16 UTC below ~1400 m altitude (Figure 8, middle row). However, above this height, the shape factor and  $\Delta AMF_i$  decrease with time: both are largest at 16 UTC and smallest at 22 UTC. The tropospheric AMF follows  $\Delta AMF_i$  above ~1400 m and also decrease with time from 1 to 0.58. Thus, the satellite measurement is more sensitive to the profile at 16 UTC than that at 22 UTC in this mountainous area. The plot over the San Gabriel Mountain area illustrates that not only boundary layer height, but also the absolute magnitude of HCHO, influence the AMF value.

Anza-Borrego Desert State Park represents an example of a case in which both boundary layer height and HCHO mixing ratio increase with time (Figure 4 and Figure 8, bottom row). In case of the lowest boundary layer height (at 16 UTC), AMF is largest (AMF=0.98). When the boundary layer height is the highest among the three time periods (at 22 UTC), the AMF is smallest (AMF=0.71). For Anza Borrego Desert State Park, total column or near surface HCHO mixing ratio affect the shape factor, which in turn leads to

an AMF that is inversely proportional to the total column or near surface HCHO mixing ratio. As shown in Figure 8, the shape factor and  $\Delta AMF_i$  above the boundary layer decrease with time, which causes a decrease in the tropospheric AMF with time.

In summary, the absolute value of the column or near-surface mixing ratio of HCHO affects the shape factor as a normalization factor, in particular the value in the free troposphere (above boundary layer), which dominates the tropospheric AMF. When the HCHO mixing ratio is low in the boundary layer, the relative importance of the absorber in the free troposphere increases. Conversely, when the HCHO mixing ratio is high in the boundary layer, the relative importance of absorber in the free atmosphere decreases. Our result suggests that a representation of the HCHO AMF using accurate fine-resolution *a priori* profile information is critical to identify HCHO plumes and to place better constraints on VOC emissions.

Although the focus of this manuscript is on the shape factor, we also investigate the impacts of aerosol loading on AMF for the 8 sites shown in Figure 4. When the aerosol optical properties from the model results are incorporated in our RT model calculations, the AMF is reduced by ~10% at the N. Main St. and Pasadena sites and by < 10% at other sites (Table 2). The aerosol optical depth, single scattering albedo, and asymmetry factor calculated from the model results for the 8 sites are about 0.5, 0.9, and 0.7, which is close

to the values suggested as most probable atmospheric conditions in the LA Basin (see Table 4 in Baidar et al., 2013). Because the model aerosol results were not thoroughly evaluated and optimized and only 8 sites were tested, the analysis of aerosol impact in this study is limited. It is possible that some of the simulated aerosol components are overestimated, because the emission inventory is not fully up to date for primary aerosol emissions and aerosol precursor gases (e.g., overestimations of black carbon and SO<sub>2</sub> by a least a factor of 3). Meanwhile, the AMF changes from the values at 16 UTC (09PT) due to diurnal variations in *a priori* profile shape range from -40% to 20% (Table 2). It is likely that the impact of aerosols on the AMF is relatively small when compared with the impact of the profile shape factor examined in this study for the LA basin. De Smedt et al. (2015) and Wang et al. (2017) also reported the importance of *a priori* profile shapes for an improvement of satellite-based HCHO retrievals in Beijing, Xianghe, Wuxi in China. Kwon et al. (2017) demonstrated that the impact of aerosol loading on HCHO AMF can be large over East Asia, in particular, for a case of Asian dust transport in contrast to our study for the LA basin.

### 3.3. Air quality application of fine-resolution geostationary HCHO columns

In this section, we illustrate the application of future geostationary HCHO retrievals to the

study of air quality, by using the WRF-Chem HCHO columns as a proxy for satellite data.

Figure 9 demonstrates the distribution of the ratio of HCHO to NO<sub>2</sub> tropospheric vertical columns from the WRF-Chem model in the LA Basin at different times of day and on weekdays and weekends for May-June 2010. For more information about the model NO<sub>2</sub>

5 columns, refer to Kim et al. (2016).

Ratios of HCHO to NO<sub>2</sub> columns provide critical information about chemical regimes relevant to controlling ozone pollution (Martin et al., 2004; Jin et al., 2017). In

Figure 9, the light blue to blue contours (HCHO/NO<sub>2</sub> < 1) represent VOC-sensitive (or VOC-limited) ozone production regimes, while the pink to the red contours (HCHO/NO<sub>2</sub>  
10 > 1) denote NO<sub>x</sub>-sensitive regimes. During weekdays in 2010, most of the LA Basin is in the VOC-sensitive regime, where a reduction in NO<sub>x</sub> emissions can cause an increase in O<sub>3</sub>. In the late afternoon during weekends, the broad polluted area becomes NO<sub>x</sub>-sensitive, so that NO<sub>x</sub> reductions lead to O<sub>3</sub> decreases.

Figure 10 shows 2000-2010 trends in surface O<sub>3</sub> from monitors in Pasadena and  
15 San Bernardino. During this decade, NO<sub>x</sub> emissions were decreasing in the LA Basin, largely due to better control of motor vehicle pollution (McDonald et al., 2012). On weekdays during this decade, there was not a declining trend in surface O<sub>3</sub> in Pasadena, while O<sub>3</sub> increased in San Bernardino. In contrast, on weekends, O<sub>3</sub> decreased between



2000 and 2010 in both Pasadena and San Bernardino. These observed O<sub>3</sub> trends are consistent with analyses of the ratio of HCHO to NO<sub>2</sub> columns, and their representation of VOC/NO<sub>x</sub> sensitivity, shown in Figure 10. Baidar et al. (2015) found that the spatial extent and the trend of higher O<sub>3</sub> during weekends than weekdays had decreased in the LA Basin because of the increased tendency of lower O<sub>3</sub> during hot weekends, especially after the 2008 economic recession.

The polar-orbiting satellite instruments that are currently available do not provide diurnally varying information on HCHO/NO<sub>2</sub> columns and VOC/NO<sub>x</sub> sensitivities, because these measurements are made once a day in either the morning or early afternoon. The discussion above makes it clear that future geostationary satellite HCHO and NO<sub>2</sub> columns will provide useful information about photochemical ozone regimes that could be used to evaluate pollution control policies.

#### 4. Summary and Conclusions

Our tests of the sensitivity of HCHO AMF to several factors confirm the importance of *a priori* HCHO profile shapes. Our study reveals that **the AMF is very sensitive to the absolute HCHO mixing ratio (or number density) in the boundary layer. Therefore, the absolute magnitude of HCHO concentration in the boundary layer** is an essential factor in determining the AMF. For the coastal LA Basin megacity studied in this work, the AMF

values are inversely proportional to the magnitude of the HCHO mixing ratios in the boundary layer. Furthermore, the AMF over land is lower in the late afternoon (15 PDT) than in the morning (09 PDT), because of increasing HCHO mixing ratios throughout the day. Therefore, diurnal updates and fine spatial resolution *a priori* profile shapes are likely  
5 to improve the retrievals of satellite-based HCHO columns.

The spatial distributions of fine-scale model HCHO columns in the LA Basin show hot spots in downtown LA around noon and enhancement and transport of the plumes to the eastern part of the Basin in the late afternoon. The ratio of HCHO to NO<sub>2</sub> columns during weekdays and weekends provides information on the chemical regimes relevant to  
10 ozone formation at various locations and times in the Basin. Future geostationary satellites (e.g., TEMPO) may provide similar information, which could be used to assess the effectiveness of existing pollution controls and could help in planning or revising air pollution control policies.

## 15 **Acknowledgements**

The NOAA Health of Atmosphere program, the NASA ROSES ACMAP (NNH14AX01I), and NASA GEO-CAPE Mission Pre-formulation Study (NNH13AW31I) supported this research. The authors thank G. Gonzalez Abad and K. Chance at Harvard SAO and H.-J. Lee at Pusan National University.

The WRF-Chem model version 3.4.1 used in this study is available at [http://www2.mmm.ucar.edu/wrf/users/download/get\\_source.html](http://www2.mmm.ucar.edu/wrf/users/download/get_source.html). We acknowledge use of MOZART-4 global model output available at <http://www.acom.ucar.edu/wrf-chem/mozart.shtml>. The CalNex field campaign data are available at

5 <http://www.esrl.noaa.gov/csd/projects/calnex/>.

## References

- Abad, G. G., X. Liu, K. Chance, H. Wang, T. P. Kurosu, and R. Suleiman (2015), Updated Smithsonian Astrophysical Observatory Ozone Monitoring Instrument (SAO OMI) formaldehyde retrieval, *Atmos. Meas. Tech.*, 8, 19-32, doi:10.5194/amt-8-19-2015.
- 5 Ahmadov, R., et al. (2015), Understanding high wintertime ozone pollution events in an oil- and natural gas-producing region of the western US, *Atmos. Chem. Phys.*, 15, 411-429, doi:10.5194/acp-15-411-2015.
- Alicke, B., U. Platt, and J. Stutz (2002), Impact of nitrous acid photolysis on the total hydroxyl radical budget during the Limitation of Oxidant Production/Pianura Padana  
10 Produzione di Ozono study in Milan, *J. Geophys. Res.-Atmos.*, 107, 8196, doi:10.1029/2000jd000075, 2002.
- Baidar, S., Oetjen, H., Coburn, S., Dix, B., Ortega, I., Sinreich, R., and Volkamer, R. (2013),  
The CU Airborne MAX-DOAS instrument: vertical profiling of aerosol extinction and  
trace gases, *Atmos. Meas. Tech.*, 6, 719-739, <https://doi.org/10.5194/amt-6-719-2013>.
- 15 Baidar, S., R. M. Hardesty, S.-W. Kim, A. O. Langford, H. Oetjen, C. J. Senff, M. Trainer,  
and R. Volkamer (2015), Weakening of the weekend ozone effect over California's  
South Coast Air Basin, *Geophys. Res. Lett.*, 42, 9457–9464,  
doi:[10.1002/2015GL066419](https://doi.org/10.1002/2015GL066419).
- Barkley, M. P., T. P. Kurosu, K. Chance, I. De Smedt, M. V. Roozendaal, A. Arneth, D.  
20 Hagberg, and A. Guenther (2012), Assessing sources of uncertainty in formaldehyde air  
mass factors over tropical South America: Implications for top-down isoprene emission  
estimates, *J. Geophys. Res.-Atmos.*, 117, D13304, doi:10.1029/2011JD016827.
- Barth, M. C., S.-W. Kim, W.C. Skamarock, A. L. Stuart, K. E. Pickering, and L. E. Ott  
(2007), Simulations of the redistribution of formaldehyde, formic acid, and peroxides in  
25 the 10 July 1996 Stratospheric-Tropospheric Experiment: Radiation, Aerosols, and

- Ozone deep convection storm, *J. Geophys. Res.-Atmos.*, 112, D13310, doi:10.1029/2006JD008046.
- Boersma, K. F., H. J. Eskes, and E. J. Brinksma (2004), Error analysis for tropospheric NO<sub>2</sub> retrieval from space, *J. Geophys. Res.-Atmos.*, 109, D04311, doi:10.1029/2003JD003962.
- 5 Borbon, A., et al. (2013), Emission ratios of anthropogenic volatile organic compounds in northern mid-latitude megacities: Observations versus emission inventories in Los Angeles and Paris, *J. Geophys. Res. Atmos.*, 118, 2041–2057, doi:[10.1002/jgrd.50059](https://doi.org/10.1002/jgrd.50059).
- De Smedt, I., Stavrou, T., Hendrick, F., Danckaert, T., Vlemmix, T., Pinardi, G., Theys, N., Lerot, C., Gielen, C., Vigouroux, C., Hermans, C., Fayt, C., Veefkind, P., Müller, J.-F., and Van Roozendael, M. (2015), Diurnal, seasonal and long-term variations of global formaldehyde columns inferred from combined OMI and GOME-2 observations, *Atmos. Chem. Phys.*, 15, 12519-12545, <https://doi.org/10.5194/acp-15-12519-2015>.
- 10 De Smedt, I., Theys, N., Yu, H., Danckaert, T., Lerot, C., Compernelle, S., Van Roozendael, M., Richter, A., Hilboll, A., Peters, E., Pedernana, M., Loyola, D., Beirle, S., Wagner, T., Eskes, H., van Geffen, J., Boersma, K. F., and Veefkind, P. (2017), Algorithm Theoretical Baseline for formaldehyde retrievals from S5P TROPOMI and from the QA4ECV project, *Atmos. Meas. Tech. Discuss.*, <https://doi.org/10.5194/amt-2017-393>, in review.
- 15 Emmons, L. K., S. Walters, P. G. Hess, J.-F. Lamarque, G. G. Pfister, D. Fillmore, C. Granier, A. Guenther, D. Kinnison, T. Laepple, J. Orlando, X. Tie, G. Tyndall, C. Wiedinmyer, S. L. Baughcum, and S. Kloster (2010), Description and evaluation of the Model for Ozone and Related chemical Tracers, version 4 (MOZART-4), *Geosci. Model Dev.*, 3, 43-67, doi:10.5194/gmd-3-43-2010, 2010.
- 20

- Fishman, J., L. T. Iraci, J. Al-Saadi, Kelly V. Chance, F. Chavez, M. Chin, P. Coble, et al. 2012. The United States' Next Generation of Atmospheric Composition and Coastal Ecosystem Measurements: NASA's Geostationary Coastal and Air Pollution Events (GEO-CAPE) Mission, *Bull. Amer. Meteorol. Soc.*, 93 (10), 1547–1566, doi:10.1175/bams-d-11-00201.1.
- 5
- González Abad, G., Liu, X., Chance, K., Wang, H., Kurosu, T. P., and Suleiman, R. (2015), Updated Smithsonian Astrophysical Observatory Ozone Monitoring Instrument (SAO OMI) formaldehyde retrieval, *Atmos. Meas. Tech.*, 8, 19-32, <https://doi.org/10.5194/amt-8-19-2015>.
- 10
- Grell, G. A., S. E. Peckham, R. Schmitz, S. A. McKeen, G. Frost, W. C. Skamarock, and B. Eder, Fully coupled “online” chemistry within WRF model, *Atmos. Environ.*, 39(37), 6957-6975, doi:10.1016/j.atmosenv.2005.04.27, 2005.
- Heckel, A., S.-W. Kim, G. J. Frost, et al. (2011), Influence of low spatial resolution a priori data on tropospheric NO<sub>2</sub> satellite retrievals, *Atmos. Meas. Tech.*, 4, 1805-1820.
- 15
- Ingmann P., Veihelmann B., Langen J., Lamarre D., Stark H., Courreges-Lacoste G. B. (2012), Requirements for the GMES Atmosphere Service and ESA's implementation concept: Sentinels-4/5 and 5p. *Remote Sens. Environ.*, 120, 58–69.
- Jin, Xiaomeng, A. M. Fiore, L. T. Murray, L. C. Valin, L. N. Lamsal, B. Duncan, K. Folkert Boersma, I. De Smedt, G. Gonzalez Abad, K. Chance, and G. S. Tonnesen (2017), Evaluating a space-based indicator of surface ozone-NO<sub>x</sub>-VOC sensitivity over midlatitude source regions and application to decadal trends. *J. Geophys. Res.*, 122, 10,439-10,461. <https://doi.org/10.1002/2017JD026720>.
- 20
- Kim, J. and the GEMS Team (2012), GEMS (Geostationary Environment Monitoring Spectrometer) onboard the GeoKOMPSAT to Monitor Air Quality in high Temporal

and Spatial Resolution over Asia-Pacific Region, Geophysical Research Abstracts Vol. 14, EGU2012-4051, 2012 EGU General Assembly.

Kim, S.-W., A. Heckel, G. J. Frost, A. Richter, J. Gleason, J. P. Burrows, S. McKeen, E.-  
Y. Hsie, C. Granier, and M. Trainer (2009), NO<sub>2</sub> columns in the western United States  
5 observed from space and simulated by a regional chemistry model and their implications  
for NO<sub>x</sub> emissions, *J. Geophys. Res.*, *114*, D11301, doi:10.1029/2008JD011343.

Kim, S.-W., S. A. McKeen, G. J. Frost, S.-H. Lee, M. Trainer, A. Richter, W. M. Angevine,  
E. Atlas, L. Bianco, K. F. Boersma, J. Brioude, J. P. Burrows, J. de Gouw, A. Fried, J.  
Gleason, A. Hilboll, J. Mellqvist, J. Peischl, D. Richter, C. Rivera, T. Ryerson, S. te  
10 Lintel Hekkert, J. Walega, C. Warneke, P. Weibring, and E. Williams (2011),  
Evaluations of NO<sub>x</sub> and highly reactive VOC emission inventories in Texas and their  
implications for ozone plume simulations during the Texas Air Quality Study 2006,  
*Atmos. Chem. Phys.*, *11*, 11361-11386, doi:10.5194/acp-11-11361-2011.

Kim, S.-W., B. C. McDonald, S. Baidar, S. S. Brown, B. Dube, R. A. Ferrare, G. J.  
15 Frost, R. A. Harley, J. S. Holloway, H.-J. Lee, et al. (2016), Modeling the weekly cycle  
of NO<sub>x</sub> and CO emissions and their impacts on O<sub>3</sub> in the Los Angeles-South Coast Air  
Basin during the CalNex 2010 field campaign, *J. Geophys. Res. Atmos.*, *121*, 1340–1360,  
doi:[10.1002/2015JD024292](https://doi.org/10.1002/2015JD024292).

Kwon, H.-A., R. J. Park, J. I. Jeong, S. Lee, G. Gonzalez Abad, T. P. Kurosu, P. I. Palmer,  
20 and K. Chance (2017), Sensitivity of formaldehyde (HCHO) column measurements  
from a geostationary satellite to temporal variation of the air mass factor in East Asia,  
*Atmos. Chem. Phys.*, *17*, 4673-4686.

Lorente, A., Folkert Boersma, K., Yu, H., Dörner, S., Hilboll, A., Richter, A., Liu, M.,  
Lamsal, L. N., Barkley, M., De Smedt, I., Van Roozendaal, M., Wang, Y., Wagner, T.,

Beirle, S., Lin, J.-T., Krotkov, N., Stammes, P., Wang, P., Eskes, H. J., and Krol, M. (2017), Structural uncertainty in air mass factor calculation for NO<sub>2</sub> and HCHO satellite retrievals, *Atmos. Meas. Tech.*, 10, 759-782, <https://doi.org/10.5194/amt-10-759-2017>.

5 Luecken, D. J., W. T. hutzell, M. L. Strum, G. A. Pouliot (2012), Regional sources of atmospheric formaldehyde and acetaldehyde, and implications for atmospheric modeling, *Atmos. Environ.*, 47, 477-490.

Martin, R. V., A. M. Fiore, and A. V. Donkelaar (2004), Space-based diagnosis of surface ozone sensitivity to anthropogenic emissions, *Geophys. Res. Lett.*, 31, L06120, doi:10.1029/2004GL019416.

10 Martin, R. V., D. D. Parrish, T. B. Ryerson, D. K. Nicks Jr., K. Chance, T. P. Kurosu, D. J. Jacob, E. D. Sturges, A. Fried, and B. P. Wert (2004), Evaluation of GOME satellite measurements of tropospheric NO<sub>2</sub> and HCHO using regional data from aircraft campaigns in the southeastern United States, *J. Geophys. Res.*, 109, D24307, doi:10.1029/2004JD004869.

15 McDonald, B. C., T. R. Dallmann, E. W. Martin, and R. A. Harley (2012), Long-term trends in nitrogen oxide emissions from motor vehicles at national, state, and air basin scales, *J. Geophys. Res.*, 117, D00V18, doi:10.1029/2012JD018304.

McDonald, B. C., D. R. Gentner, A. H. Goldstein, and R. A. Harley (2013), Long-term trends in motor vehicle emissions in U.S. urban areas, *Environ. Sci. Technol.*, 46, 10022-20 10031, doi:10.1021/es401034z.

McDonald, B. C., Z. C. McBride, E. W. Martin, and R. A. Harley (2014), High-resolution mapping of motor vehicle carbon dioxide emissions, *J. Geophys. Res. Atmos.*, 119, 5283-5298, doi:10.1002/2013JD021219.



- Millet, D. B., D. J. Jacob, J. F. Boersma, T.-M. Fu, T. P. Kurosu, K. Chance, C. L. Heald, and A. Guenther (2008), Spatial distribution of isoprene emissions from North America derived from formaldehyde column measurements by the OMI satellite sensor, 113, D02307, doi:10.1029/2007JD008950.
- 5 Palmer, P. I., D. J. Jacob, K. Chance, R. V. Martin, R. J. D. Spurr, T. Kurosu, I. Bey, R. Yantosca, A. Fiore, and Q. Li (2001), Air-mass factor formulation for differential optical absorption spectroscopy measurements from satellites and application to formaldehyde retrievals from GOME, *J. Geophys. Res.*, 106, 17,147-17,160.
- Platt, U. and J. Stutz (2008), Differential Optical Absorption Spectroscopy: Principles and  
10 Applications, ISBN 978-3540211938, Springer, Heidelberg, New York, 2008.
- Pollack, I. B., et al. (2012), Airborne and ground-based observations of a weekend effect in ozone, precursors, and oxidation products in the California South Coast Air Basin, *J. Geophys. Res.*, 117, D00V05, doi:10.1029/2011JD016772.
- Ryerson, T. B., et al. (2013), The 2010 California Research at the Nexus of Air Quality  
15 and Climate Change (CalNex) field study, *J. Geophys. Res.*, 118, 5830-5866, doi:10.1002/jgrd.50331.
- Russell, A. R., A. E. Perring, L. C. Valin, E. J. Bucsela, E. C. Browne, P. J. Wooldridge, and R. C. Cohen (2011), A high spatial resolution retrieval of NO<sub>2</sub> column density from OMI: method and evaluation, *Atmos. Chem. Phys.*, 11, 8543-8554,  
20 <https://doi.org/10.5194/acp-11-8543-2011>.
- Scott, K. I. and M. T. Benjamin (2003), Development of biogenic volatile organic compounds emission inventory for the SCOS97-NARSTO domain, *Atmos. Environ.*, 37, Supplement No. 2, S39-S49.

- Spurr, R. J. D. (2006), VLIDORT: A linearized pseudo-spherical vector discrete ordinate radiative transfer code for forward model and retrieval studies in multilayer multiple scattering media, *Journal of Quantitative Spectroscopy & Radiative Transfer*, 102, 316-342.
- 5 Starvrouk, T., J.-F. Muller, M. Bauwens, I. De Smedt, M. Van Roozendael, M. De Maziere, C. Vigouroux, F. Hendrick, M. George, C. Clerbaux, P.-F. Coheur, and A. Guenther (2015), How consistent are top-down hydrocarbon emissions based on formaldehyde observations from GOME-2 and OMI?, *Atmos. Chem. Phys.*, 15, 11861-11884.
- 10 Stockwell, W. R., F. Kirchner, and M. Kuhn (1997), A new mechanism for regional atmospheric chemistry modeling, *J. Geophys. Res.*, 102, 25,847-25,879.
- Stutz, J. and Platt, U. (1996), Numerical analysis and estimation of the statistical error of differential optical absorption spectroscopy measurements with least-squares methods, *Appl. Optics*, 35, 6041-6053.
- 15 Stutz, J. and Platt, U. (1997), Improving long-path differential optical absorption spectroscopy with a quartz-fiber mode mixer, *Appl. Optics*, 36, 1105-1115.
- US EPA, Office of Air Quality and Planning and Standards, Emissions, Monitoring and Analysis Division, Emissions Inventory Group, Research Park Triangle, NC (2008), Documentation for the 2005 Mobile National Emissions Inventory, Version 2.
- 20 US EPA (2015a), Technical Support Document EPA's 2011 National-scale Air Toxics Assessment, 2011 NATA TSD, <https://www.epa.gov/sites/production/files/2015-12/documents/2011-nata-tsd.pdf>.

US EPA (2015b), Office of Air Quality and Planning and Standards, Emissions, Monitoring and Analysis Division, Emissions Inventory Group, Research Park Triangle, NC, 2011 National Emissions Inventory, version 2 Technical Support Document.

5 Veefkind, J. P., et al. (2012), TROPOMI on the ESA Sentinel-5 Precursor: A GMES mission for global observations of the atmospheric composition for climate, air quality and ozone layer applications. *Remote Sensing of Environment* 120, 70-83.

10 Veihelmann, B., Meijer Y., Ingmann P., Koopman R., Wright N., Bazalgette Courrèges-Lacoste G., et al. The Sentinel-4 mission and its atmospheric composition products. In Proceedings of the 2015 EUMETSAT meteorological satellite conference. France, 21–25 September 2015.

15 Wang, Y., Beirle, S., Lampel, J., Koukouli, M., De Smedt, I., Theys, N., Li, A., Wu, D., Xie, P., Liu, C., Van Roozendaal, M., Stavrou, T., Müller, J.-F., and Wagner, T. (2017), Validation of OMI, GOME-2A and GOME-2B tropospheric NO<sub>2</sub>, SO<sub>2</sub> and HCHO products using MAX-DOAS observations from 2011 to 2014 in Wuxi, China: investigation of the effects of priori profiles and aerosols on the satellite products, *Atmos. Chem. Phys.*, 17, 5007-5033, <https://doi.org/10.5194/acp-17-5007-2017>.

20 Warneke, C., P. Veres, J. S. Holloway, J. Stutz, C. Tsai, S. Alvarez, B. Rappenglueck, F. C. Fehsenfeld, M. Graus, J. B. Gilman, and J. A. de Gouw (2011), Airborne formaldehyde measurements using PTR-MS: calibration, humidity dependence, inter-comparison and initial results, *Atmos. Meas. Tech.*, 4, 2345-2358.

Wolfe, G. M., Kaiser, J., Hanisco, T. F., Keutsch, F. N., de Gouw, J. A., Gilman, J. B., Graus, M., Hatch, C. D., Holloway, J., Horowitz, L. W., Lee, B. H., Lerner, B. M., Lopez-Hilifiker, F., Mao, J., Marvin, M. R., Peischl, J., Pollack, I. B., Roberts, J. M., Ryerson, T. B., Thornton, J. A., Veres, P. R., and Warneke, C. (2016), Formaldehyde

production from isoprene oxidation across NO<sub>x</sub> regimes, *Atmos. Chem. Phys.*, 16, 2597-2610, <https://doi.org/10.5194/acp-16-2597-2016>.

Zhu, L., D. J. Jacob, L. J. Mickley, E. A. Marais, D. S. Cohan, Y. Yoshida, B. N. Duncan, G. Gonzalez Abad, and K. V. Chance (2014), Anthropogenic emissions of highly reactive volatile organic compounds in eastern Texas inferred from oversampling of satellite (OMI) measurements of HCHO columns. *Environ. Res. Lett.*, 9 (11), 114004.

Zhu, L., D. J. Jacob, P. S. Kim, J. A. Fisher, K. Yu, and coauthors (2016), Observing atmospheric formaldehyde (HCHO) from space: validation and intercomparison of six retrievals from four satellites (OMI, GOME2A, GOME2B, OMPS) with SEAC<sup>4</sup>RS aircraft observations over the southeast US, *Atmos. Chem. Phys.*, 16, 13477-13490.

Zoogman, P., X. Liu, R.M. Suleiman, W.F. Pennington, D.E. Flittner, J.A. Al-Saadi, B.B. Hilton, D.K. Nicks, M.J. Newchurch, J.L. Carr, S.J. Janz, M.R. Andraschko, A. Arola, B.D. Baker, B.P. Canova, C. Chan Miller, R.C. Cohen, J.E. Davis, M.E. Dussault, D.P. Edwards, J. Fishman, A. Ghulam, G. González Abad, M. Grutter, J.R. Herman, J. Houck, D.J. Jacob, J. Joiner, B.J. Kerridge, J. Kim, N.A. Krotkov, L. Lamsal, C. Li, A. Lindfors, R.V. Martin, C.T. McElroy, C. McLinden, V. Natraj, D.O. Neil, C.R. Nowlan, E.J. O'Sullivan, P.I. Palmer, R.B. Pierce, M.R. Pippin, A. Saiz-Lopez, R.J.D. Spurr, J.J. Szykman, O. Torres, J.P. Veefkindz, B. Veihelmann, H. Wang, J. Wang, K. Chance (2017), Tropospheric Emissions: Monitoring of Pollution (TEMPO), *J. Quantitative Spectroscopy and Radiative Transfer*, 186, 17-39, <http://dx.doi.org/10.1016/j.jqsrt.2016.05.008>

## Figure captions

Figure 1. Diurnal variations of ground-based observations (black filled circles with solid lines) of HCHO and the corresponding model simulations (lines without symbols) in Pasadena (34.1370°N, 118.1254°W) averaged for weekdays (left) and weekends (right) during May-June 2010. All model simulations utilized the fuel-based NO<sub>x</sub> and CO emissions in Kim et al. (2016). The red solid line shows the results utilizing the VOC emissions from the top-down approach in Borbon et al. (2013), the red dashed line denotes the same model settings represented by the red solid line (top-down approach) except for zero biogenic VOC (BVOC) emissions, the blue solid line represents the model results using the VOC emissions from NEI05 (as in Kim et al., 2016), and the light blue line shows the model output using the VOC emissions from NEI11.

Figure 2. The flight path of NOAA WP-3 (top) and the spatial distribution of vertical profiles of aircraft observed and model simulated potential temperature (middle) and HCHO (bottom) in the LA Basin on May 4, 2010. The black filled circles and red solid lines/symbols represent the observations and model results, respectively.

Figure 3. The spatial distributions of air mass factors from the radiative transfer model calculations (left) and HCHO columns (right) in the LA Basin at 16 UTC (top), 19 UTC (middle), and 22 UTC (bottom) on May 4, 2010. The black filled circles are included as points of further investigations, representing background, urban cores, and downwind regions.

Figure 4. Vertical profiles of HCHO are shown for various points of interest (red symbols on a Google map). Blue, orange, and magenta lines represent 16, 19, and 22 UTC (or 09, 12, 15 PDT), respectively on May 4, 2010. The altitude AGL is shown. The same plot with the unit of molecules  $\text{cm}^{-3}$  is shown in the Supplementary Material.

Figure 5. Vertical profiles of HCHO averaged for the AMF value intervals (as in legends) at 16, 19, and 22 UTC (left to right) are displayed. Thick lines with symbols are for averages and thin dotted lines are for one standard deviation values. The altitude AGL is shown. The same plot with the unit of molecules  $\text{cm}^{-3}$  is shown in the Supplementary Material.

Figure 6. The relationship between the AMF and model HCHO volume mixing ratio is demonstrated. Different colors denote different times. The HCHO mixing ratio at ~200 m altitude AGL is plotted. The same plot with the unit of molecules  $\text{cm}^{-3}$  is shown in the Supplementary Material.

5

Figure 7. Comparison of HCHO mixing ratios at 4 km x 4 km resolution with mixing ratios at coarser resolutions of (a) 8 km x 8 km, (b) 12 km x 12 km, (c) 20 km x 20 km, (d) 36 km x 36 km, (e) 48 km x 48 km, (f) 100 km x 100 km, (g) 200 km x 200 km, and (h) 300 km x 300 km. One-to-one line is shown in black.

10

Figure 8. Vertical profiles of (left) shape factor and scattering weight and (right)  $\Delta AMF_i$  (discrete increment of AMF) at North Pacific Ocean, San Gabriel Mountains, and Anza Borrego Desert State Park. Scattering weights multiplied by geometric AMF are shown. Dashed lines and solid lines with symbols in the left panel denote the scattering weight and shape factor, respectively. Total (or tropospheric) AMF values are shown in legends in the right panel.

15

Figure 9. Spatial distributions of the ratios of the model HCHO column to NO<sub>2</sub> column during weekdays (left) and weekends (right) at 09 PDT, 12 PDT, and 15 PDT for May-June 2010. The light pink to red colored contours denote the area under the NO<sub>x</sub>-limited chemical regime.

5

Figure 10. Decadal O<sub>3</sub> trends in Pasadena and San Bernardino during weekdays (red) and weekends (blue) are shown. The linear least square fits of O<sub>3</sub> for Wednesday and Sunday are plotted in dashed lines.

10

15

20



## Table captions

Table 1. Percentage (%) of intense HCHO plumes retained as the spatial resolution is  
5 changed from 4 km. Each column shows the fraction of the plumes retained at coarser  
resolutions. Here the plume is defined by the area in which the HCHO mixing ratio is  
greater than the reference HCHO volume mixing ratio (VMR) (1-6 ppb) at 4 km resolution.  
For example, the second column shows how much area at 8-200 km resolution has a HCHO  
VMR > 1 ppb when compared with the area with VMR > 1 ppb at 4 km resolution.  
10 Similarly, the last column shows how often a model HCHO VMR is greater than 6 ppb at  
8-200 km resolution compared with the same plume of VMR > 6 ppb at 4 km resolution;  
all coarser resolutions (8-200 km) fail to capture this most intense plume. Only model  
HCHO results at 200 m above ground level at 19 UTC (12 PDT) are used. The areas with  
HCHO VMRs greater than 1, 2, 3, 4, 5, or 6 ppb are 92800, 29136, 12832, 4256, 848, or  
15 64 km<sup>2</sup>, respectively in the original simulations at 4 km resolution. The area of the domain  
is 143856 km<sup>2</sup>.

Table 2. Summary of air mass factors at 8 locations at 16-22 UTC (09-15 PDT). The results  
without/with aerosols impacts are also shown.

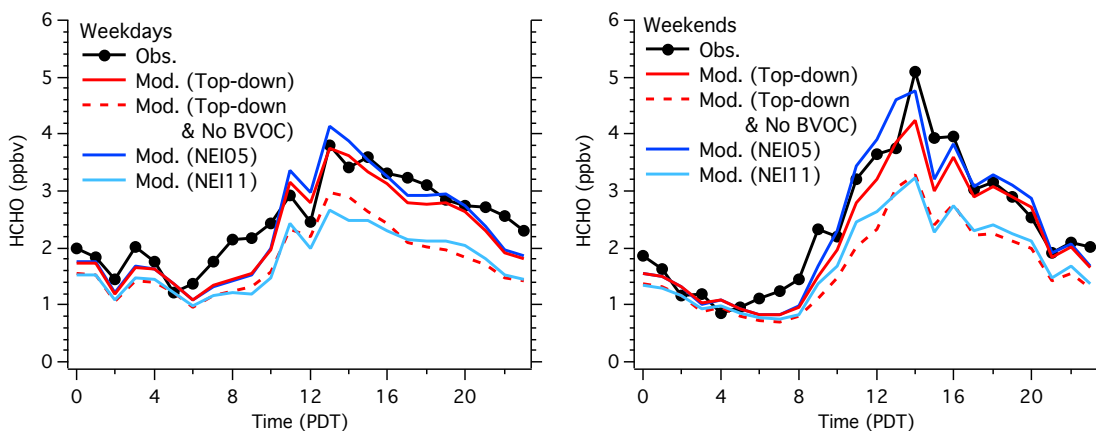
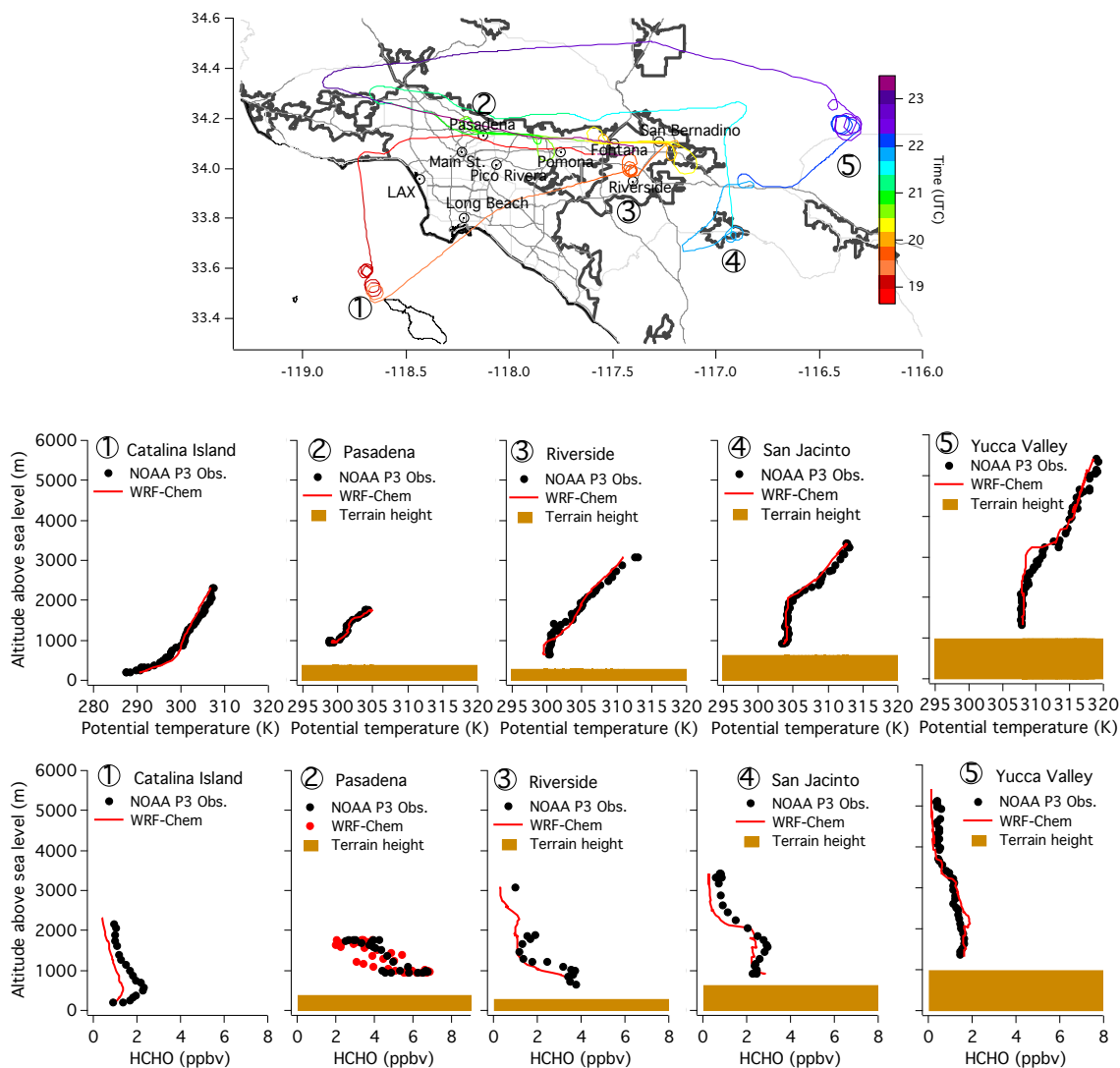


Figure 1. Diurnal variations of ground-based observations (black filled circles with solid lines) of HCHO mixing ratio and the corresponding model simulations (lines without symbols) in Pasadena (34.1370°N, 118.1254°W) averaged for weekdays (left) and weekends (right) during May-June 2010. All model simulations utilized the fuel-based NO<sub>x</sub> and CO emissions in Kim et al. (2016). The red solid line shows the results utilizing the VOC emissions from the top-down approach in Borbon et al. (2013), the red dashed line denotes the same model settings represented by the red solid line (top-down approach) except for zero biogenic VOC (BVOC) emissions, the blue solid line represents the model results using the VOC emissions from NEI05 (as in Kim et al., 2016), and the light blue line shows the model output using the VOC emissions from NEI11.



5 Figure 2. The flight path of the NOAA WP-3 aircraft (top) and the spatial distribution of vertical profiles observed on the aircraft and simulated by the model for potential temperature (middle) and HCHO (bottom) in the LA Basin on May 4, 2010. The black filled circles and red solid lines/symbols represent the observations and model results, respectively.

10

15

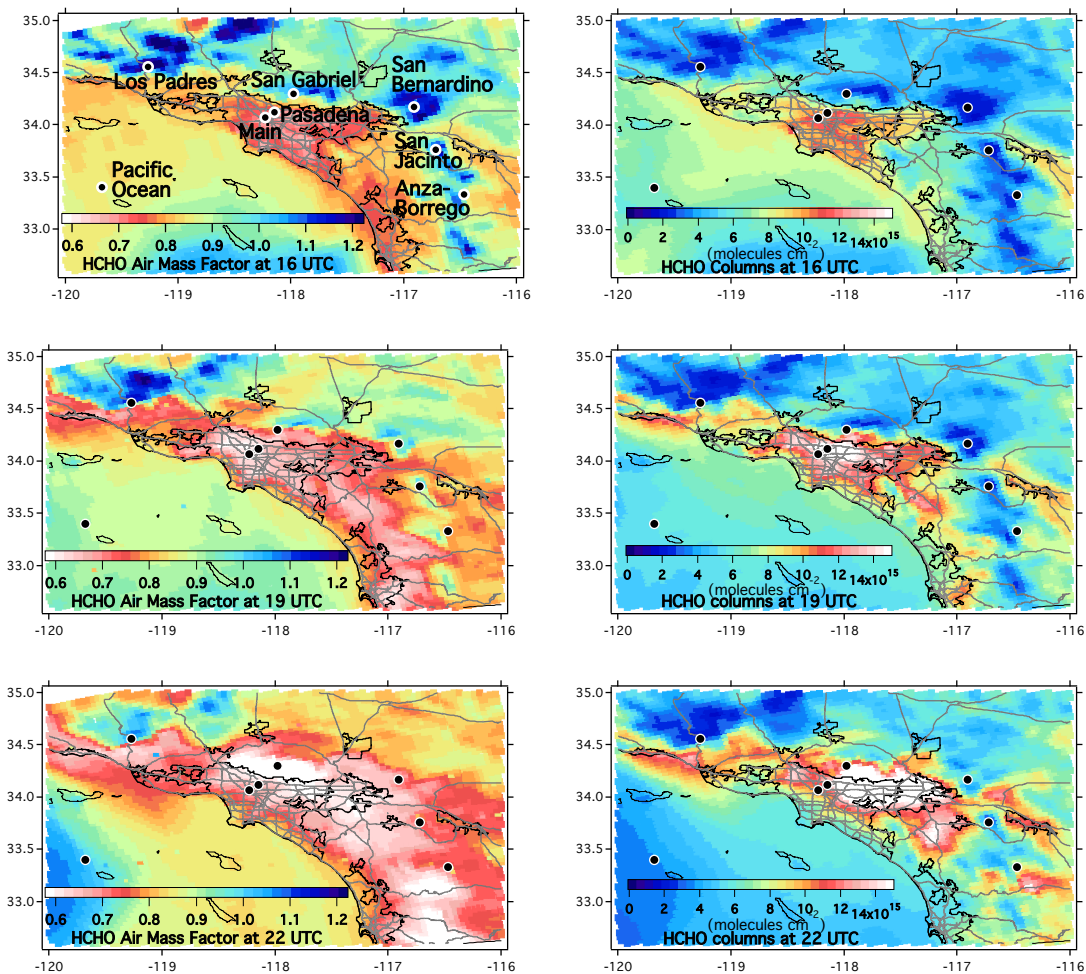


Figure 3. The spatial distributions of air mass factors from the radiative transfer model calculations (left) and HCHO columns (right) in the LA Basin at 16 UTC (top), 19 UTC (middle), and 22 UTC (bottom) on May 4, 2010. The black filled circles are included as points of further investigations, representing background, urban cores, and downwind regions.

10

15

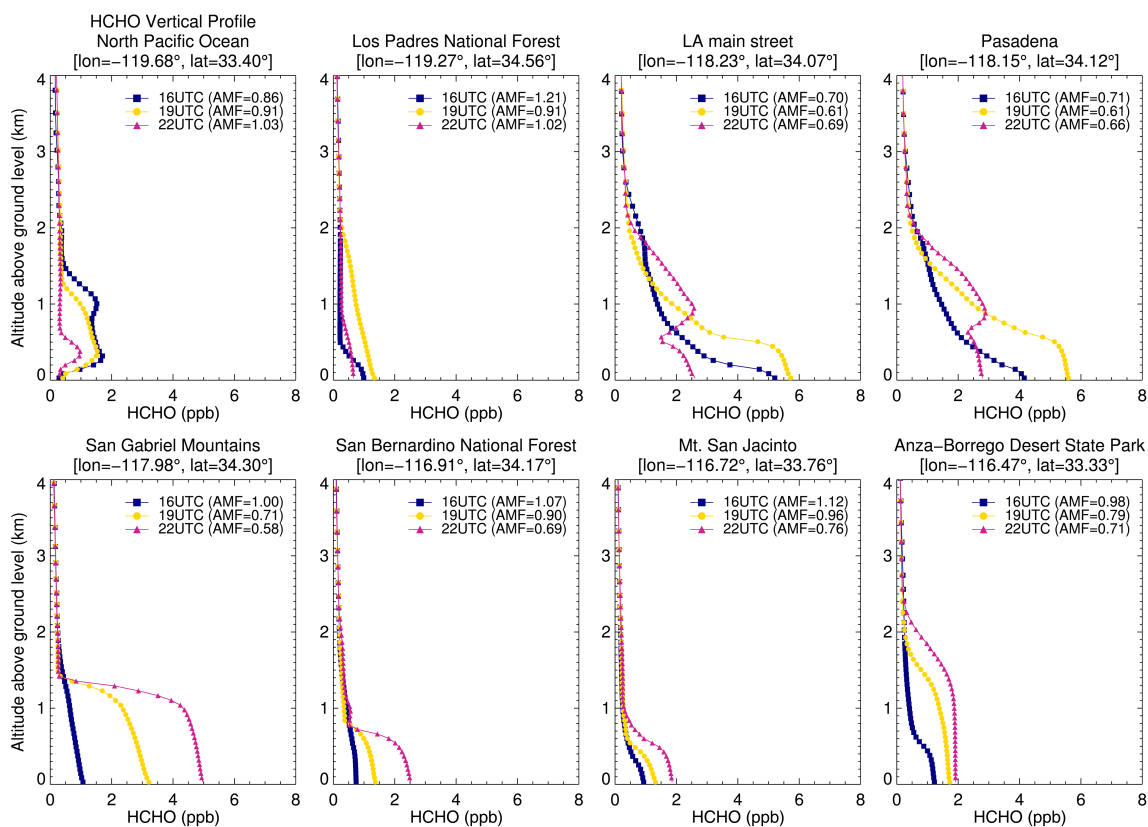
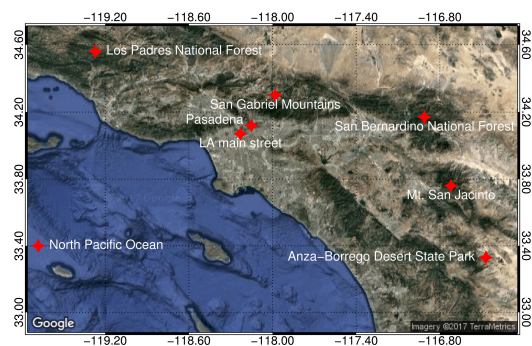


Figure 4. Vertical profiles of HCHO mixing ratio are shown for various points of interest (red symbols on a Google map). Blue, orange, and magenta lines represent 16, 19, and 22 UTC (or 09, 12, 15 PDT), respectively on May 4, 2010. The altitude AGL is shown. The same plot with the unit of molecules  $\text{cm}^{-3}$  is shown in the Supplementary Material.

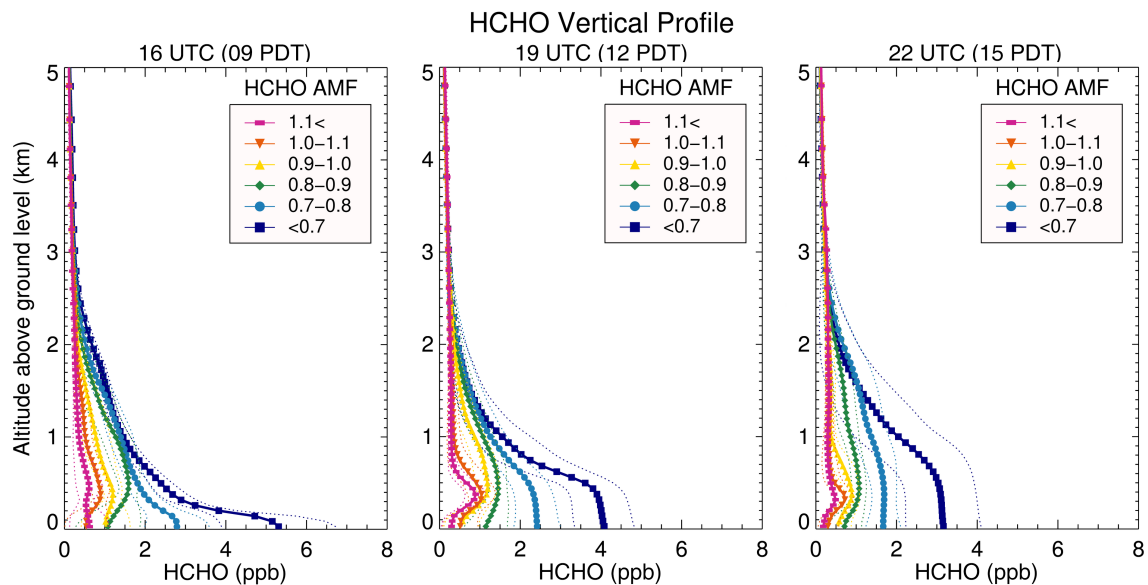


Figure 5. Vertical profiles of HCHO mixing ratio averaged for the AMF value intervals (as in legends) at 16, 19, and 22 UTC (left to right) are displayed. Thick lines with symbols are for averages and thin dotted lines are for one standard deviation values. The altitude AGL is shown. The same plot with the unit of molecules  $\text{cm}^{-3}$  is shown in the Supplementary Material.

10

15

20

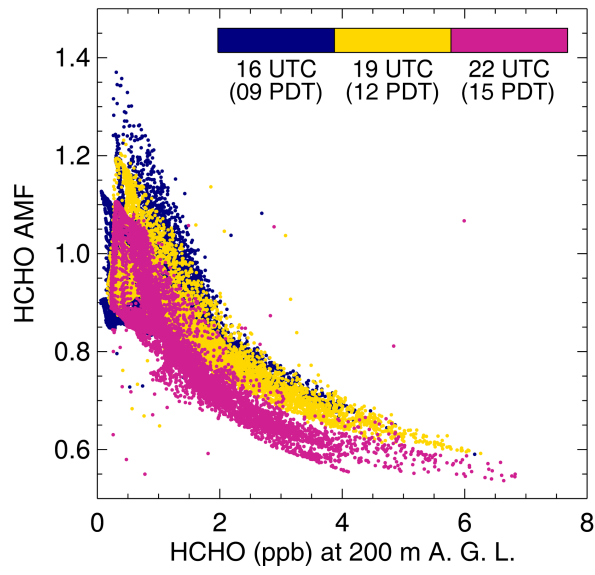


Figure 6. The relationship between the AMF and model HCHO volume mixing ratio is demonstrated. Different colors denote different times. The HCHO mixing ratio at ~200 m altitude AGL is plotted. The same plot with the unit of molecules  $\text{cm}^{-3}$  is shown in the  
5 Supplementary Material.

10

15

20

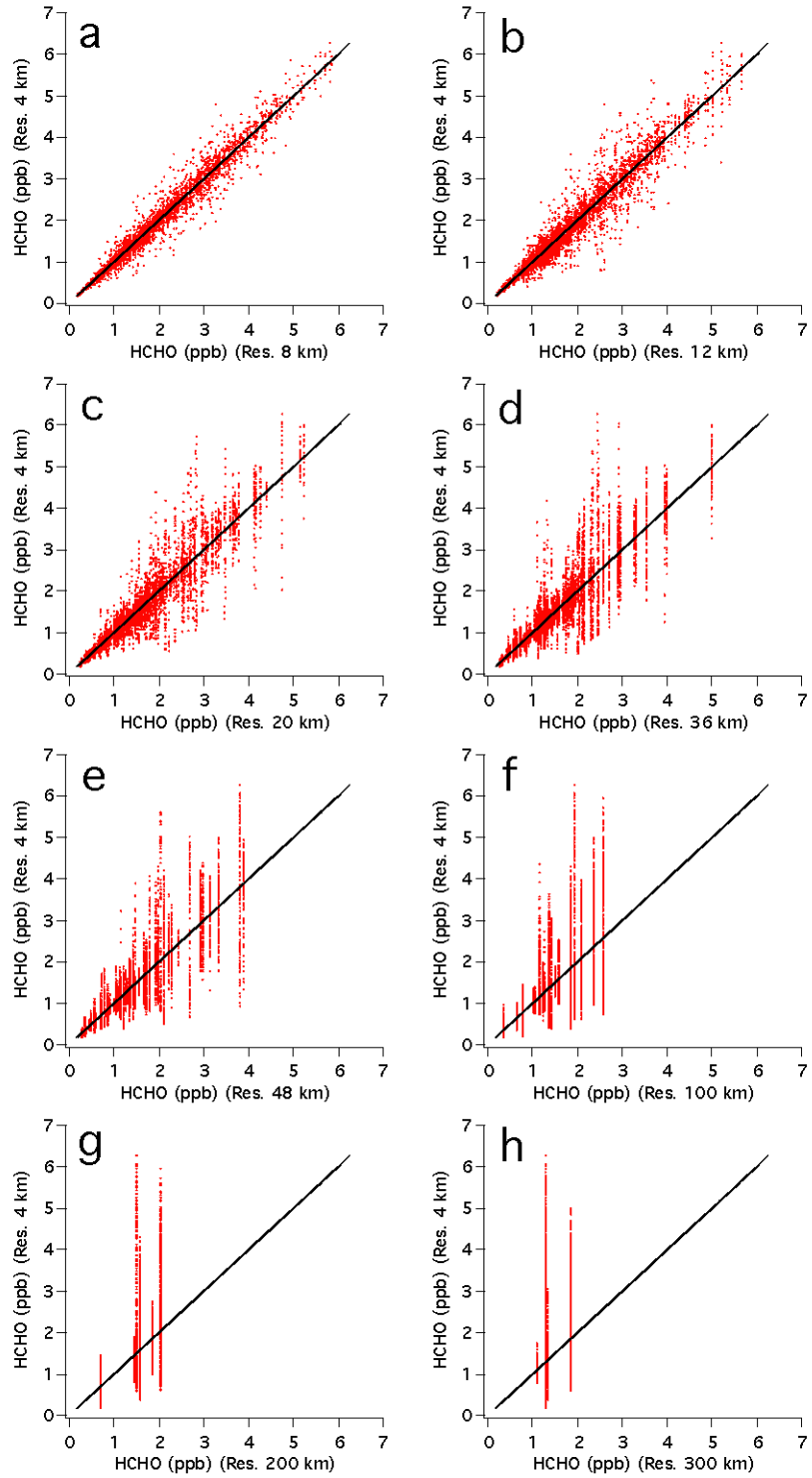


Figure 7. Comparison of HCHO mixing ratios at 4 km x 4 km resolution with mixing ratios at coarser resolutions of (a) 8 km x 8 km, (b) 12 km x 12 km, (c) 20 km x 20 km, (d) 36 km x 36 km, (e) 48 km x 48 km, (f) 100 km x 100 km, (g) 200 km x 200 km, and (h) 300 km x 300 km. One-to-one line is shown in black.



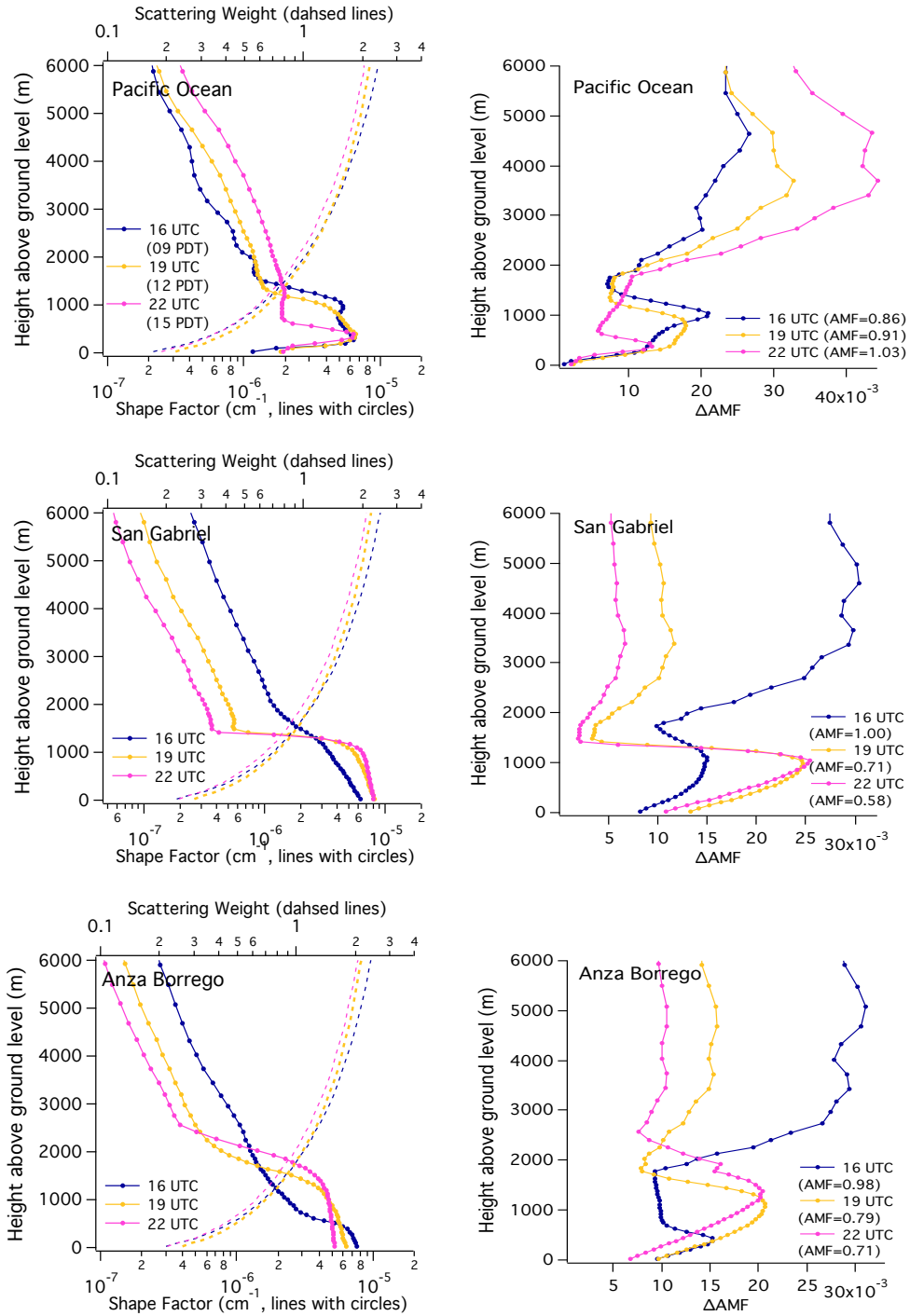


Figure 8. Vertical profiles of (left) **shape** factor and scattering weight and (right)  $\Delta AMF_i$  (discrete increment of AMF) at North Pacific Ocean, San Gabriel Mountains, and Anza Borrego Desert State Park. Scattering weights multiplied by geometric AMF are shown. **Dashed lines and solid lines with symbols in the left panel denote the scattering weight and shape factor, respectively. Total (or tropospheric) AMF values are shown in legends in the right panel.**

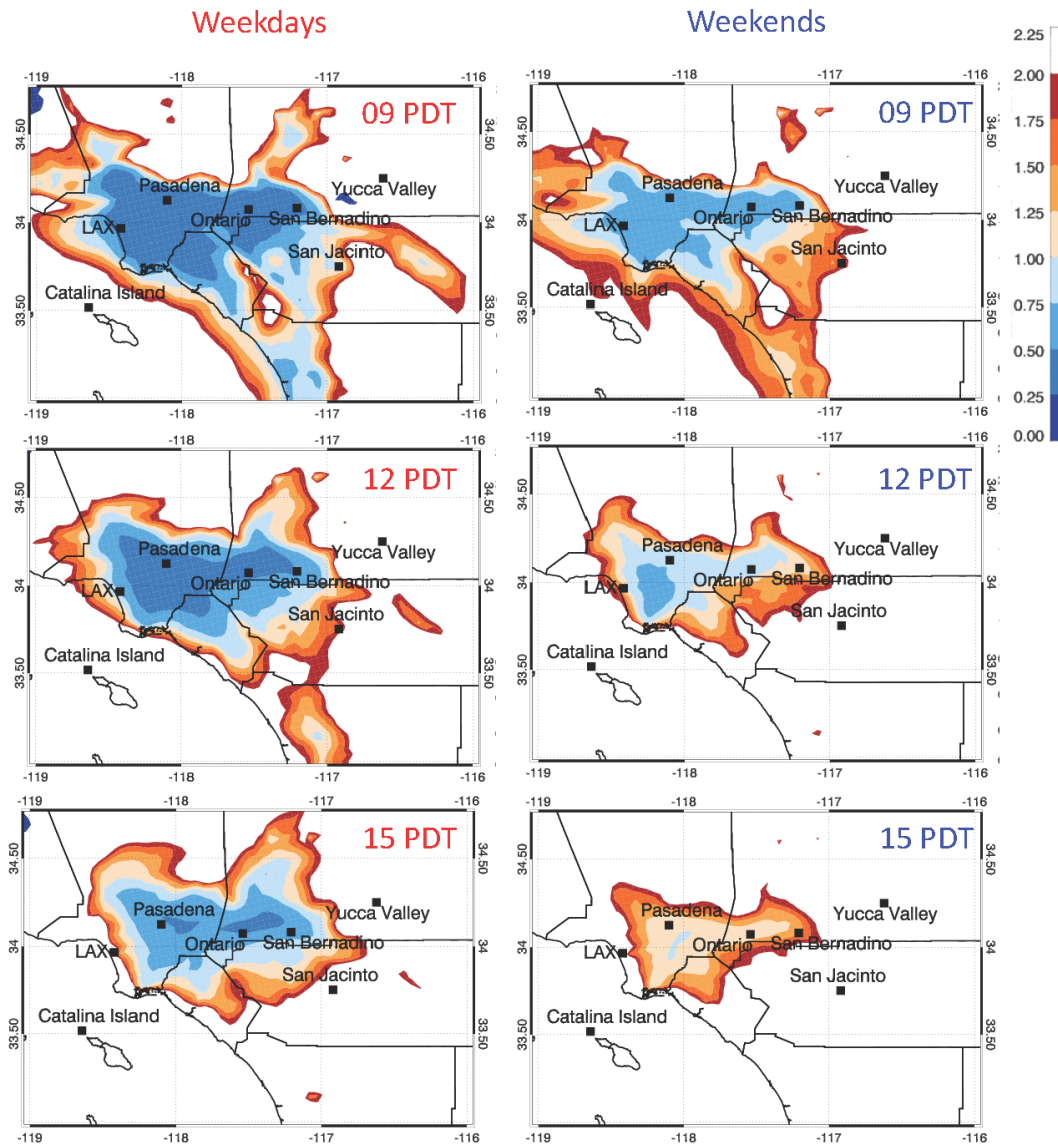


Figure 9. Spatial distributions of the ratios of the model HCHO column to  $\text{NO}_2$  column during weekdays (left) and weekends (right) at 09 PDT, 12 PDT, and 15 PDT for May-June 2010. The light pink to red colored contours denote the area under the  $\text{NO}_x$ -limited chemical regime, while blue contours denote VOC-limited regions.

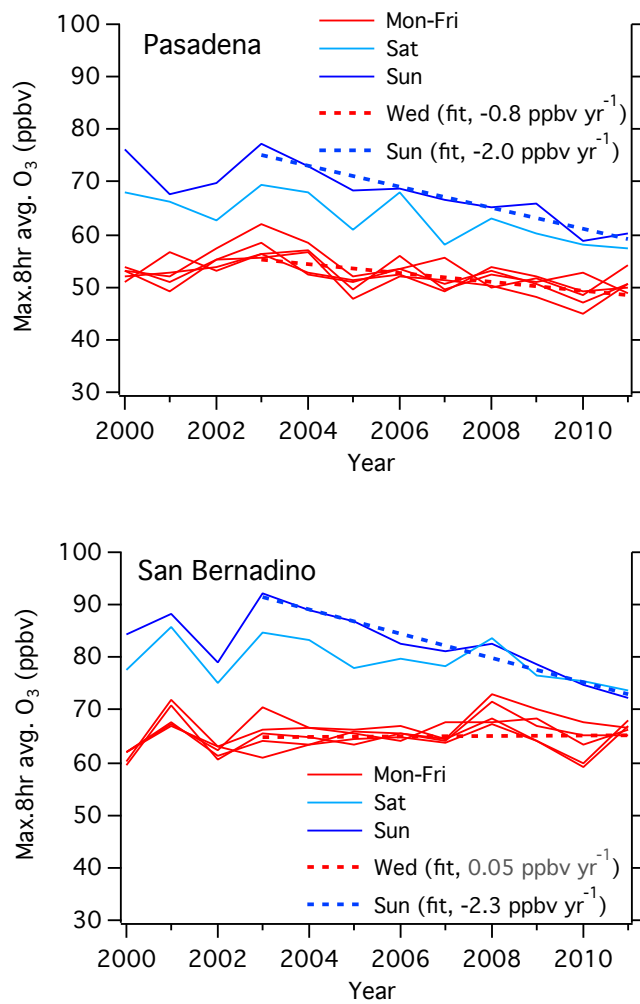


Figure 10. Decadal O<sub>3</sub> trends in Pasadena and San Bernardino during weekdays (red) and weekends (blue) are shown. The linear least square fits of O<sub>3</sub> for Wednesday and Sunday are plotted in dashed lines.

5

10

Table 1. Percentage (%) of intense HCHO plumes retained as the spatial resolution is changed from 4 km. Each column shows the fraction of the plumes retained at coarser resolutions. Here the plume is defined by the area in which the HCHO mixing ratio is greater than the reference HCHO volume mixing ratio (VMR) (1-6 ppb) at 4 km resolution. For example, the second column shows how much area at 8-200 km resolution has a HCHO VMR > 1 ppb when compared with the area with VMR > 1 ppb at 4 km resolution. Similarly, the last column shows how often a model HCHO VMR is greater than 6 ppb at 8-200 km resolution compared with the same plume of VMR > 6 ppb at 4 km resolution; all coarser resolutions (8-200 km) fail to capture this most intense plume. Only model HCHO results at 200 m above ground level at 19 UTC (12 PDT) are used. The areas with HCHO VMRs greater than 1, 2, 3, 4, 5, or 6 ppb are 92800, 29136, 12832, 4256, 848, or 64 km<sup>2</sup>, respectively in the original simulations at 4 km resolution. The area of the domain is 143856 km<sup>2</sup>.

Spatial resolution (km)	Reference HCHO volume mixing ratio (ppb) at 4 km resolution					
	1	2	3	4	5	6
8	98	95	91	84	79	0
12	97	92	85	73	79	0
20	97	86	72	67	58	0
36	97	82	52	29	0	0
48	96	72	51	0	0	0
100	96	62	0	0	0	0
200	89	56	0	0	0	0
300	53	46	0	0	0	0

15

20

Table 2. Summary of air mass factors at 8 locations at 16-22 UTC (09-15 PDT). The results without/with aerosols impacts are also shown.

Location	16 UTC (09PDT)		19 UTC (12 PDT)		22 UTC (15 PDT)	
	Aerosol		Aerosol		Aerosol	
	X	O	X	O	X	O
N. Pacific Ocean	0.86	0.75	0.90	0.85	1.03	0.99
Los Padres	1.21	1.15	0.90	0.86	1.02	1.00
Main St.	0.70	0.60	0.61	0.54	0.69	0.62
Pasadena	0.71	0.62	0.60	0.53	0.66	0.58
San Gabriel	1.00	0.93	0.71	0.65	0.58	0.51
San Bernardino	1.07	1.02	0.89	0.86	0.69	0.66
San Jacinto	1.12	1.07	0.95	0.93	0.76	0.73
Anza-Borrego	0.98	0.91	0.79	0.75	0.71	0.66

## Supplementary Material

Impact of high-resolution *a priori* profiles on satellite-based formaldehyde retrievals by Si-Wan Kim<sup>1,2,3</sup>, Vijay Natraj<sup>4</sup>, Seoyoung Lee<sup>3</sup>, Hyeong-Ahn Kwon<sup>5</sup>, Rokjin Park<sup>5</sup>, Joost de Gouw<sup>1,2</sup>, Gregory Frost<sup>1</sup>, Jhoon Kim<sup>3</sup>, Jochen Stutz<sup>6</sup>, Michael Trainer<sup>1</sup>, Catalina Tsai<sup>6</sup>, and Carsten Warneke<sup>1,2</sup>

<sup>1</sup> NOAA Earth System Research Laboratory, Chemical Sciences Division, Boulder, CO 80305, USA

10 <sup>2</sup> Cooperative Institute for Research in Environmental Sciences, University of Colorado, Boulder, CO, USA

<sup>3</sup> Department of Atmospheric Sciences, Yonsei University, Seoul, South Korea

<sup>4</sup> Jet Propulsion Laboratory, California Institute of Technology, Pasadena, CA, USA

<sup>5</sup> Department of Earth and Environmental Sciences, Seoul National University, Seoul, South Korea

15 <sup>6</sup> Department of Atmospheric Sciences, University of California, Los Angeles, CA, USA

Correspondence to: Si-Wan Kim ([siwan.kim@noaa.gov](mailto:siwan.kim@noaa.gov))

20

The Supplementary Material includes List of Figures and Figure S1 to S8.

25

30

## List of Figures

Figure S1. Spatial distributions of AMFs from RT model calculations for HCHO retrieval at 19 UTC (12 PDT) in the LA Basin: (a) AMF in the control case (CTL) using top-down VOC emissions, (b) same as CTL except for constant surface pressure, and (c) same as CTL except for NEI11 VOC emission inventory.

Figure S2. Histogram of (left) differences between the default AMF and the AMF derived using constant surface pressure, and (right) differences between the default AMF and the AMF derived using the NEI11 inventory (with lower VOC emissions than our default inventory) at 19 UTC (12 PDT).

Figure S3. Comparison of the AMF in the OMI operational product (filled square at the center of the OMI swath) with the AMF from this study. An OMI pixel is 24 km x 13 km at nadir and the pixel size increases on either side of this point. The OMI AMF is about 1 on average (blue colors in the color scale used here).

Figure S4. Vertical profiles of HCHO number density are shown for various point of interest, similar to Figure 4 in the main manuscript.

Figure S5. Diurnal variations (06 PDT to 16 PDT) of vertical profiles of HCHO mixing ratio, potential temperature, wind speed, and wind direction over the North Pacific Ocean region.

Figure S6. Vertical profiles of HCHO number density averaged for the AMF value intervals (shown in the legends) at 16, 19, and 22 UTC (left to right) as a function of altitude above ground level. Thick lines with symbols are averages and thin dotted lines are one standard deviations. This figure is similar to Figure 5 in the main manuscript except that HCHO number density is shown instead of mixing ratio.

Figure S7. The relationship between the HCHO AMF and model HCHO volume mixing ratio at ~ 200 m altitude. Different colors denote different times. This figure is similar to Figure 6 in the main manuscript except that HCHO number density is shown instead of HCHO mixing ratio.

Figure S8. (Top) AMF at 8 sites in the domain at 9, 12, and 15 PDT without/with aerosol impacts. Filled (open) square denote AMF with (without) aerosol impacts. (Bottom) changes in AMF (%) with time. Black (red) open square denotes changes of AMF between 9 and 12 PDT (15PDT).

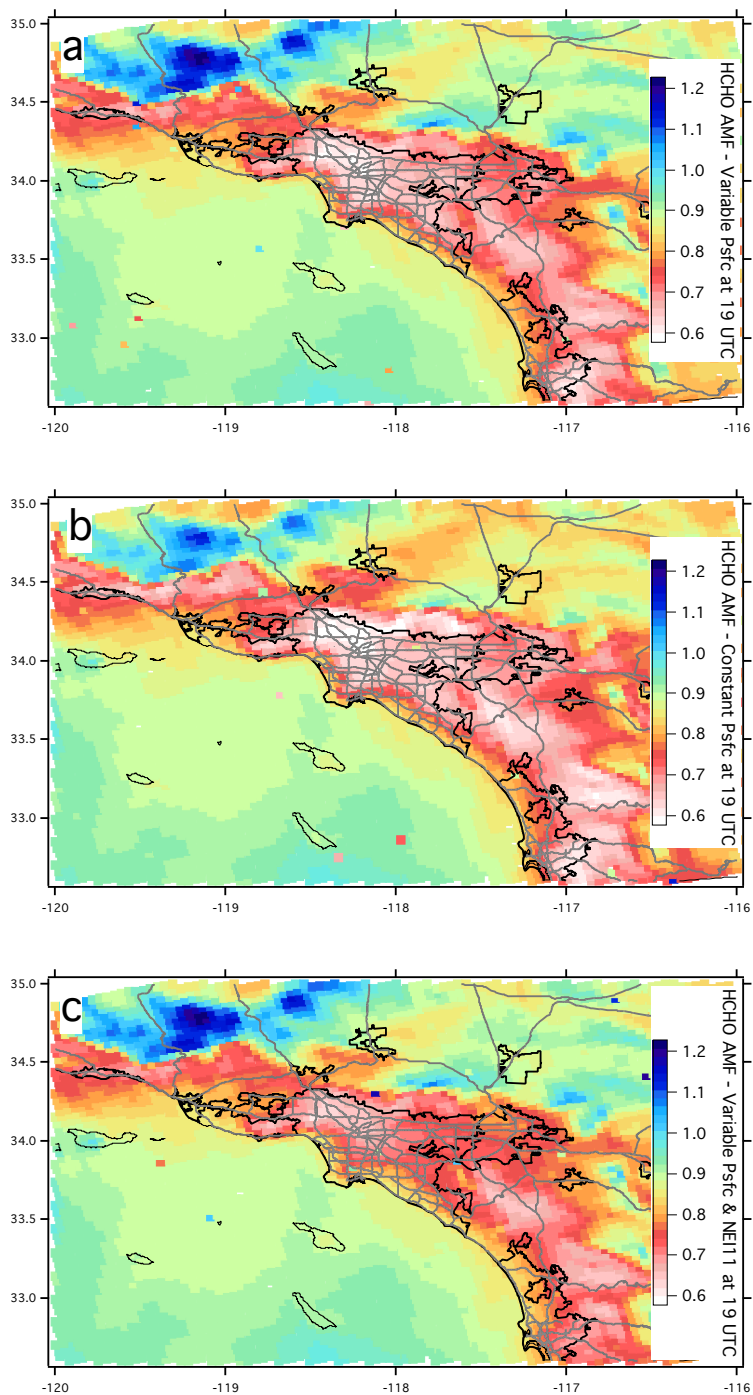


Figure S1. Spatial distributions of AMFs from RT model calculations for HCHO retrieval at 19  
 5 UTC (12 PDT) in the LA Basin: (a) AMF in the control case (CTL) using top-down VOC  
 emissions, (b) same as CTL except for constant surface pressure, and (c) same as CTL except for  
 NEI11 VOC emission inventory.



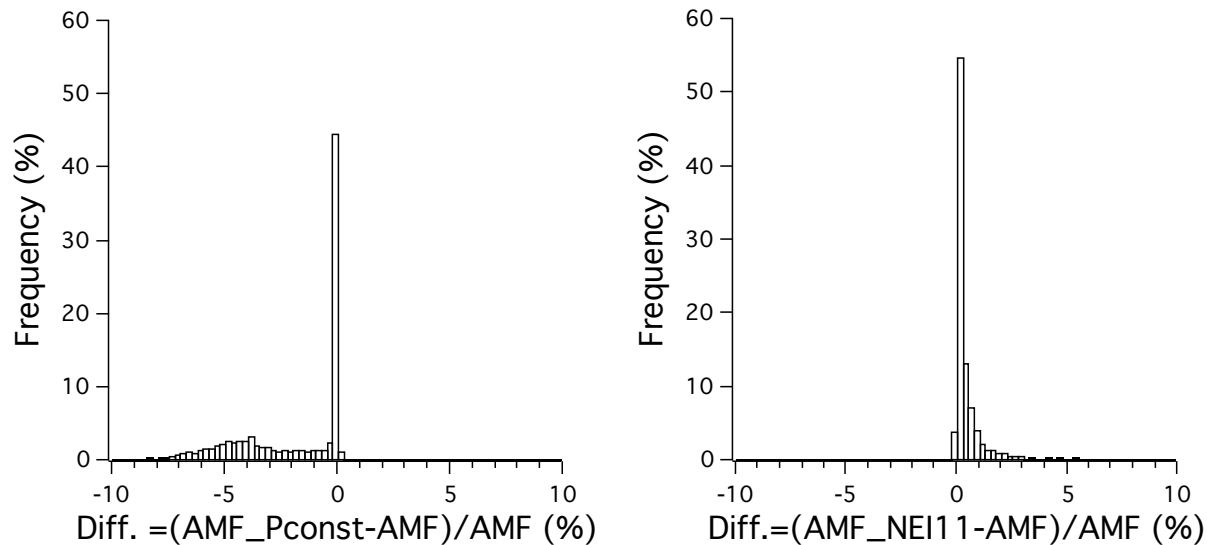


Figure S2. Histogram of (left) differences between the default AMF and the AMF derived using constant surface pressure, and (right) differences between the default AMF and the AMF derived using the NEI11 inventory (with lower VOC emissions than our default inventory) at 19 UTC (12 PDT).

5

10

15

20

25

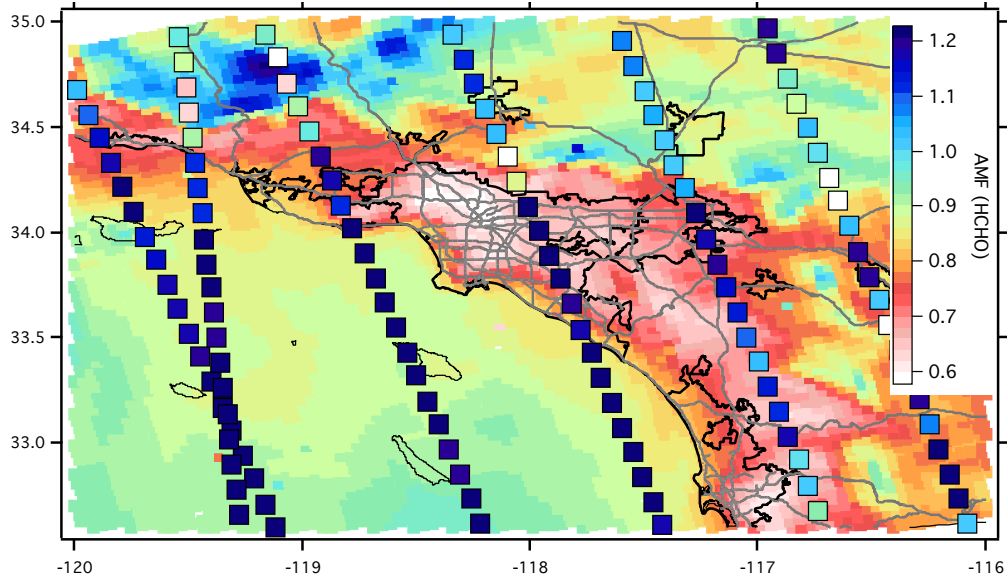


Figure S3. Comparison of the AMF in the OMI operational product (filled square at the center of the OMI swath) with the AMF from this study. An OMI pixel is 24 km x 13 km at nadir and the pixel size increases on either side of this point. The OMI AMF is about 1 on average (blue colors in the color scale used here).

5

10

15

20

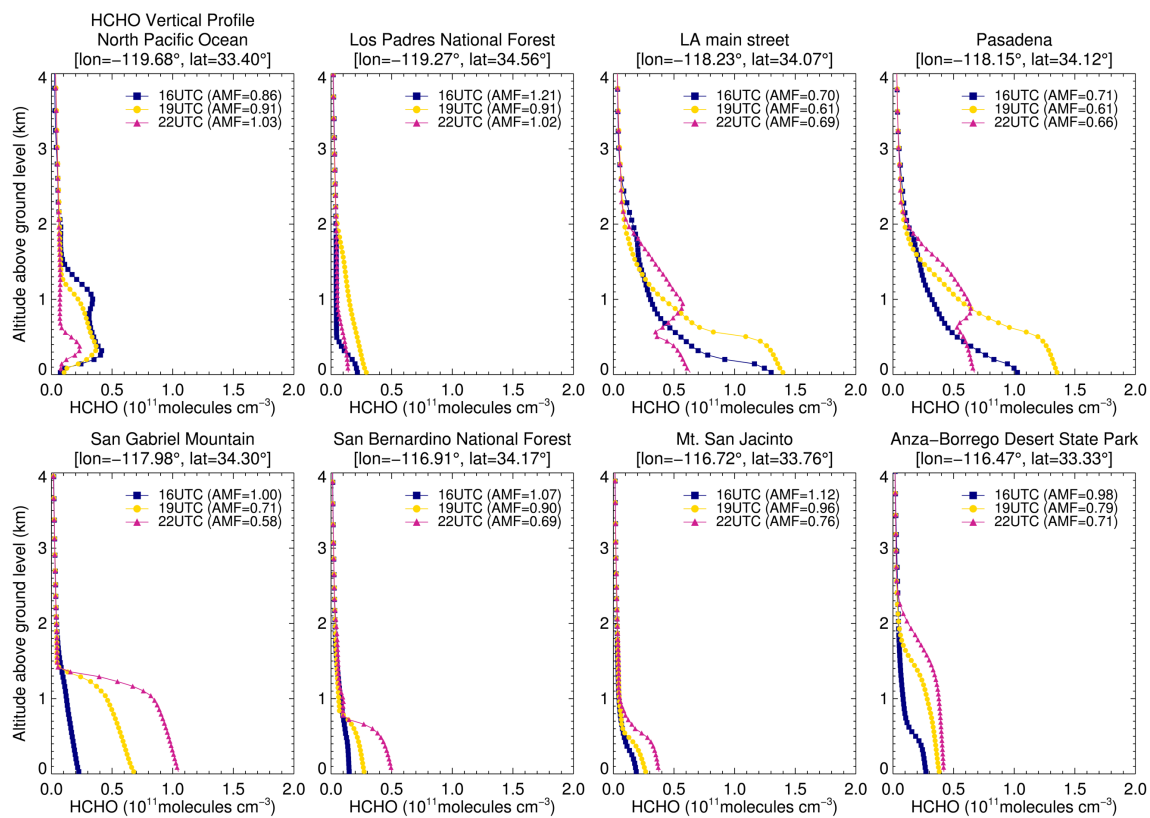


Figure S4. Vertical profiles of HCHO number density are shown for various point of interest, similar to Figure 4 in the main manuscript.

5

10

15

20

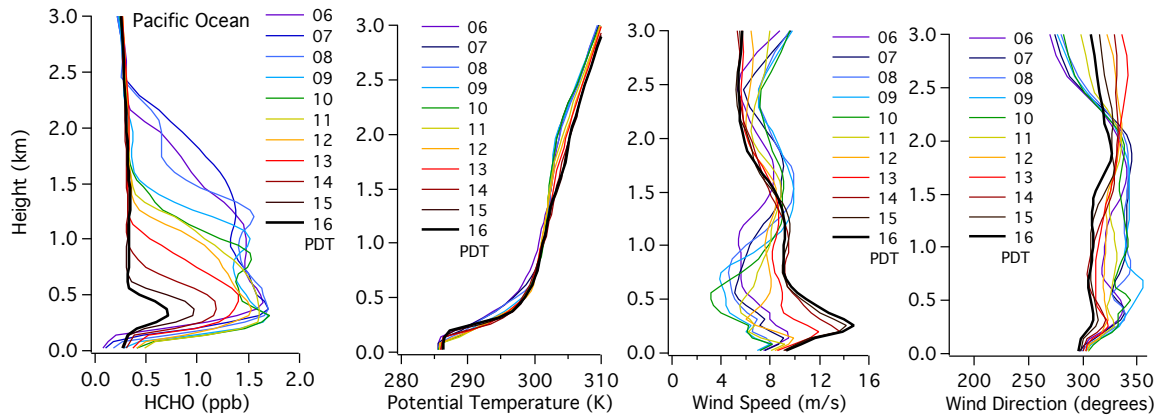


Figure S5. Diurnal variations (06 PDT to 16 PDT) of vertical profiles of HCHO mixing ratio,  
 5 potential temperature, wind speed, and wind direction over the North Pacific Ocean region.

10

15

20

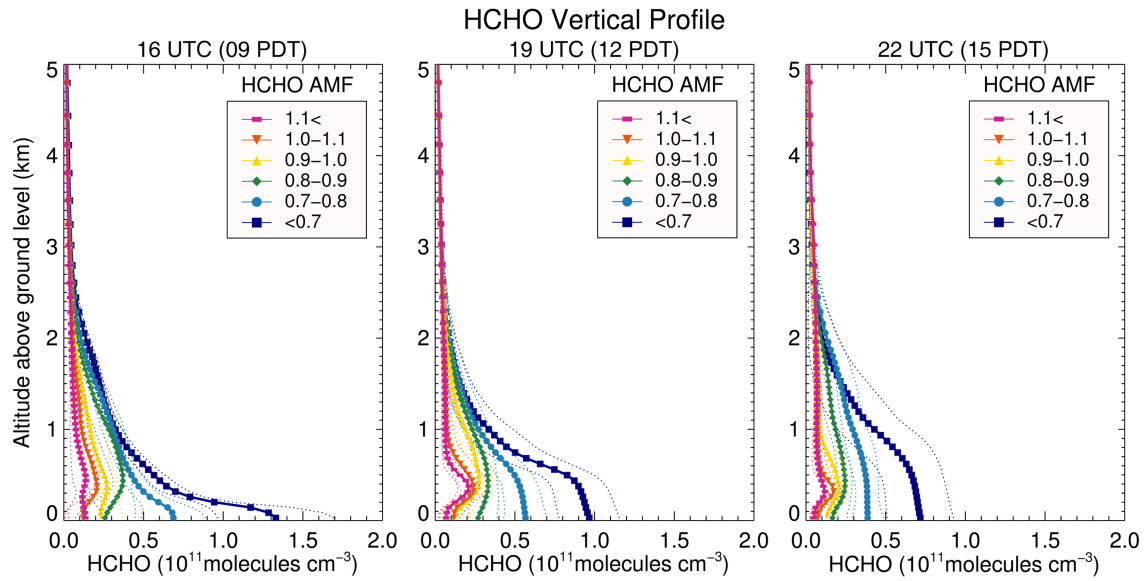


Figure S6. Vertical profiles of HCHO number density averaged for the AMF value intervals (shown in the legends) at 16, 19, and 22 UTC (left to right) as a function of altitude above ground level. Thick lines with symbols are averages and thin dotted lines are one standard deviations. This figure is similar to Figure 5 in the main manuscript except that HCHO number density is shown instead of mixing ratio.

5

10

15

20

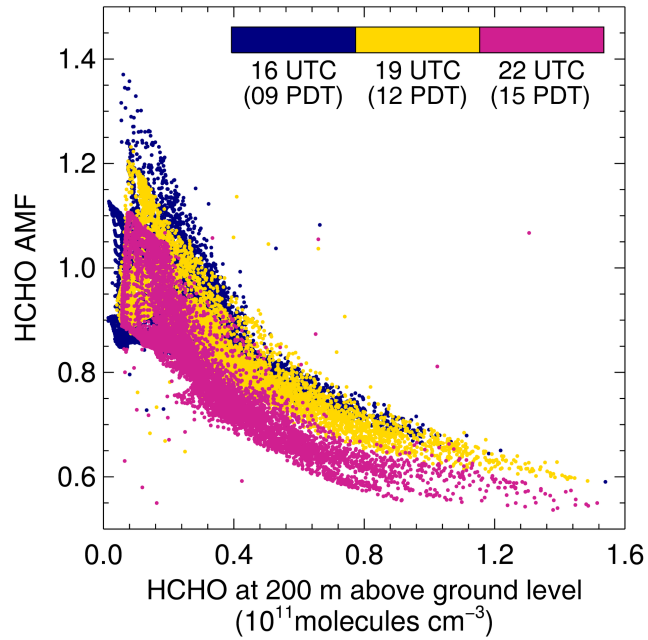


Figure S7. The relationship between the HCHO AMF and model HCHO volume mixing ratio at ~ 200 m altitude. Different colors denote different times. This figure is similar to Figure 6 in the main manuscript except that HCHO number density is shown instead of HCHO mixing ratio.

5

10

15

20

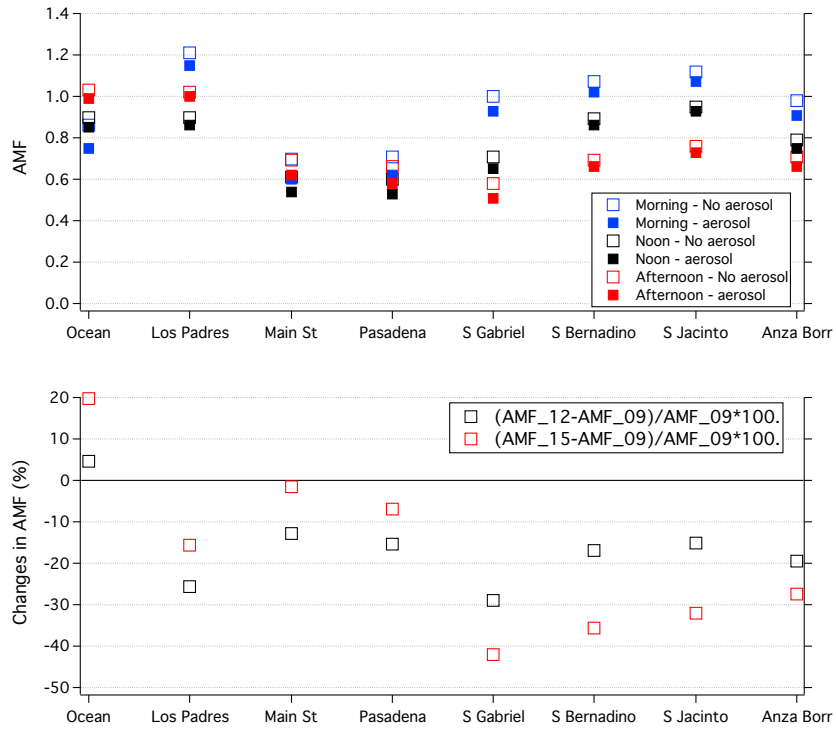


Figure S8. (Top) AMF at 8 sites in the domain at 9, 12, and 15 PDT without/with aerosol impacts. Filled (open) square denote AMF with (without) aerosol impacts. (Bottom) changes in AMF (%) with time. Black (red) open square denotes changes of AMF between 9 and 12 PDT (15PDT).

5

10

15

20